2018-01-01

Fracture Mechanics Of Heterogeneous Composites

Md Fazle Rabbi
University of Texas at El Paso, fazlerbb@gmail.com

FRACTURE MECHANICS OF HETEROGENEOUS COMPOSITES

MD FAZLE RABBI

Master's Program in Mechanical Engineering

APPROVED:

Calvin M. Stewart, Ph.D., Chair

Yirong Lin, Ph.D.

Soheil Nazarian, Ph.D.

Charles Ambler, Ph.D.
Dean of the Graduate School

Dedication

To my beloved Mother, whose love is all that I am today

FRACTURE MECHANICS OF HETEROGENEOUS COMPOSITES

by

MD FAZLE RABBI, BSME

THESIS

Presented to the Faculty of the Graduate School of

The University of Texas at El Paso

in Partial Fulfillment

of the Requirements

for the Degree of

MASTER OF SCIENCE

Department of Mechanical Engineering

THE UNIVERSITY OF TEXAS AT EL PASO

May 2018

Acknowledgments

I would first and foremost like to express my deepest gratitude and respect to my advisor Dr. Calvin M Stewart, Assistant Professor, Department of Mechanical Engineering at UTEP, for his inspiration, motivation and continuous support. This research would not be possible without his guidance. His door was always open whenever I needed any direction during developing ideas, experimenting in the lab or even writing my thesis. He patiently mentored me throughout the process, providing encouragement to solve in-situ problems and constantly inspire me with his broad vision. I wholeheartedly appreciate his time and effort to make this research successful.

I would like to thank the funding agencies, Sandia National Laboratories and Southern Plains Transportation Center (SPTC) for giving the opportunity to continue the exciting research on the diverse fields of heterogeneous composites. I am thankful to Michael J. Kaneshige from Sandia for providing insight, knowledge, and expertise on Polymer bonded explosive material. I like to thank Jaime Moya and Vieta M. Crain from Sandia for their cooperation. I am truly thankful to Professor Dr. Soheil Nazarian, Director of CTIS, UTEP, Dr. Imad Abdallah, Victor Garcia for providing their extensive support throughout my period with the SPTC project.

I am grateful to my research team member, Robert Mach for his enthusiastic participation and cooperation despite his busy class and lab schedule. I also like to extend my thanks to the members of our MERG group for their support, direction, and suggestions at various stage of this research.

I am truly thankful to my thesis committee members, Professor Dr. Soheil Nazarian, Professor Dr. Yirong Lin for their thoughtful suggestions and guidance. Their profound comments regarding my research help me to build more structured and organized thesis. I appreciate their time from the deepest of my heart.

I also greatly acknowledge the chair of the Mechanical Engineering Department, Professor Dr. Ahsan R. Chowdhury for providing the facility and proper environment to conduct research and arranging useful training on time to time basis. My gratitude goes to all the stuff of the

Department of Mechanical Engineering and cSETR center for their cooperation during this study period.

Finally, I like to express my respects, appreciations, and gratefulness from the bottom of my heart to my family, my Mother, Father, Sister and my Wife for their unconditional love. Their inspiration, untiring support build all my confidence and strength to finish this research work.

Abstract

The increasing application of composite materials due to their ubiquitous advance in terms of mechanical and thermal properties has brought attention to the fracture mechanics of the materials possessing heterogeneity. Recent investigations have focused on the micro- and macro-mechanism of fracture in heterogeneous composites (HCs). In this study, the fracture mechanics of the two HCs: Polymer bonded explosive (PBX) simulant and hot mixed asphalt (HMA) are evaluated on the macroscopic scale. It is an interest of Sandia National Laboratory to examine the fracture resistance of PBXs, particularly those of varying composition and subjected to aging. In this research, a batch of PBX simulants are manufactured in the laboratory environment and the fracture resistance is experimentally investigated. Primarily, a simulant composition of 80 wt.% soda lime glass beads (SLGB) and 20 wt.% high impact Polystyrene 825 (HIPS) is prepared to perform Brazilian disk tests to characterize the tensile and compressive properties. Fracture toughness and energy tests are performed in the semi-circular bending (SCB) configuration on 80, 81, 82, and 83 wt.% SLGB compositions. Digital image correlation (DIC) is performed to record the surface displacements and calculate surface strains during testing. The micromechanical behavior of ductile and brittle fracture is observed using digital microscopy and scanning electron microscopy of the fracture surface. It is found that fracture behavior is heavily depended on the microstructural heterogeneous distribution of particulate polymer matrix, micro-voids/cracks, and interfacial bonding energy. In the consecutive section, a proposal on the thermomechanical behavior of hot mixed asphalt (HMA) at low temperature is presented. There is a need to elucidate the thermomechanical fracture resistance of HMAs employed in the pavement. These materials are highly heterogeneous, with batch-to-batch variations outside of these observed in classic structure materials (such as structural alloys or even concrete). The impact of weather on these materials (HMAs) is one of the primary research focuses of the Southern Plains Transportation Center. On that interest, this proposal is prepared to investigate the thermal stress and thermal mismatch of HMA subjected to cooling. HMA specimens will manufacture according to TxDOT

standard. This proposal includes a plan to perform the indirect tensile test and thermal stress restrained specimen test for single edge prismatic specimen on several HMAs at varying temperature to acquire a master curve and low-temperature fracture properties. The application of DIC system will enable us to observe crack initiation, propagation, and nucleation as well as the thermal and mechanical strains, and thermal contraction coefficient within asphalt specimens. This plan of the proposal also includes the integration of Infrared (IR) thermography with DIC in order to observe the thermal mismatch gradient. A method will develop to sync the DIC cameras and the IR cameras to take images of the asphalt specimens simultaneously and then it will post-process using MATLAB software. These approaches of analysis and the series of testing protocols will enable us to investigate the thermomechanical response of HMAs and to achieve a sustainable solution for a better understanding of HMAs complex interactions of fracture mechanics at weather extremes.

Table of Contents

List of Tables

List of Figures

List of Illustrations

Chapter 1: Fracture Resistance of Polymer-Bonded Explosive Simulant using the Semi-Circular Bending Test

Introduction

Polymer bonded explosives (PBXs) are a complex class of particulate composite material that is formed by two constituent materials: energetic crystals in a polymer binder [1]. These PBXs may also consist of a small percent of additives like plasticizers, oxidizers, and antioxidants that are added to the ratio composition to improve the explosive output and decrease the effects of aging [2]. The energetic crystals typically comprise about 60 to 98% of the total mass of the composite, depending on the desired explosive output [3]. PBXs are relatively insensitive to shock. This is due to the viscoelastic-plastic polymer binder that absorbs mechanical energy to prevent friction between the energetic crystals that would result in detonation. Fracture resistance is a key metric to evaluate the sensitivity of solid explosives. To improve the insensitivity characteristics of PBXs, credible simulants that replicate the mechanical behavior and fracture resistance of real PBX have been developed. The fracture resistance of the simulants could then be safely optimized to determine the ideal composition for future PBXs.

Many quantitative studies on the fracture resistance of PBXs have been performed. Chen et al performed SCB fracture tests on a generic PBX simulant to calculated plain strain fracture toughness and determined that the dominant fracture mode is decohesion of the particle-binder interface [4]. The researchers then performed a comparative study of the fracture toughness of three-point bending, semi-circular bending (SCB), and flattened Brazilian disc tests and determined that the fracture toughness of PBX is consistent irrespective to specimen geometry [7]. The team went on to applied high-speed DIC to characterize the K_{Ic} as a function of strain rate using a split Hopkinson pressure bar and found that the fracture resistance increases with the strain rate [8]. Liu et al went on to measure the variation of fracture toughness as a function of crack growth [9]. A craze zone is observed where sizable aligned polymer molecules form bridges at the crack tip. Fracture characterization and prediction using the fracture toughness is not sufficient

since the craze zone redistributes stress creating a large process zone such that the local stress-intensity factor may not even exist [9].

Polymer bonded explosives exhibit a viscoelastic-plastic response, where cracks tend to grow through the polymer binder, along with the binder-particle interfaces. This tortuous cracking process creates a large plastic zone that exceeds the small-scale plasticity limitation of linear elastic fracture mechanics (LEFM). Fracture toughness has continued to be applied to analyze the fracture resistance of PBXs despite the deficits of LEFM [4]-[9]. As an alternative, elastic-plastic fracture mechanics (EPFM) can be introduced to measure the fracture resistance. In EPFM, fracture resistance is measured using the fracture energy, G_f better known as the critical strain energy release rate, J_c. Efforts to explore the utility of as a fracture resistance metric for PBXs are underway [10], [11].

Table 1 – Survey of Fracture Parameters of PBX and PBX simulants

Name	Type	K_{Ic} ($MPa\sqrt{m}$)	G_f ($KJ \cdot m^{-2}$)	Reference
RM-03-AG	Mock 89.5/10.5	0.602±0.030 0.659±0.026	0.016 0.042	[11]
LX-17	PBX 92.5/7.5	0.317±0.024 0.366±0.019	0.012 0.030	
PMMA	Plexiglas	1.749±0.325	1.157	
PBS 9501	Mock 95/5	N/A	0.111	[10]
EDC1032	Mock 85/15	N/A	0.657	
EDC1037	Mock 91/9	N/A	0.0153	
Mock 900-21	Mock 94/6	0.200±0.010	N/A	[9]
N/A	Mock-95/15	0.523±0.038 0.498±0.023 0.530±0.010	N/A	[8]
JOB-9003	PBX	0.240±0.010	N/A	[6]
JO-9159	PBX	0.170±0.010		
JB-9014	PBX	0.370±0.010		

Note: N/A means not available

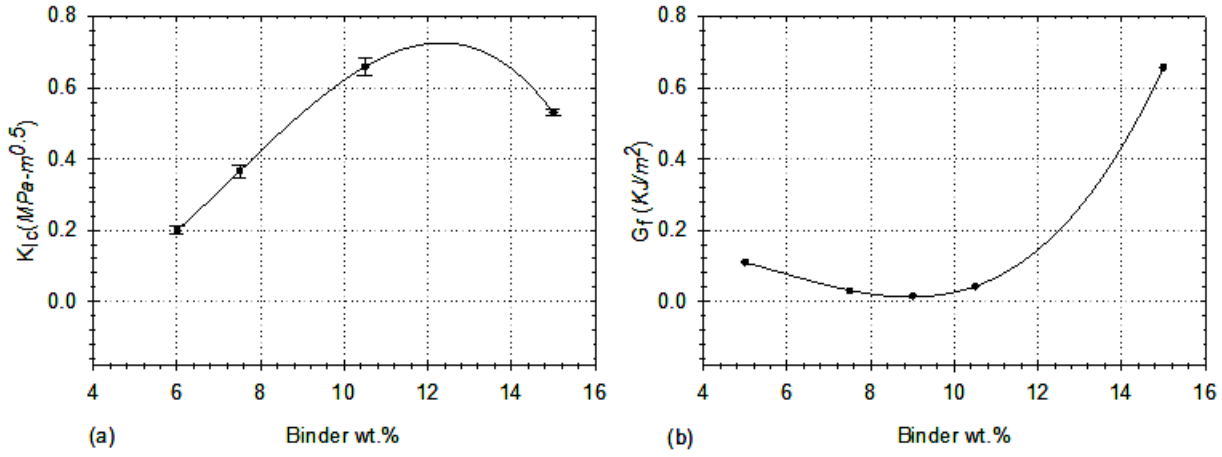

Figure 1 – Comparative plot of different *PBXs* with (a) fracture toughness range and binder weight percentage, (b) fracture energy and binder weight percentage

Fracture toughness and energy with different binder weight percentages, composed from several dissimilar mock PBXs, are stated in Table 1. Most of the mechanical property data available in the literature for PBX is of simulants. The PBX simulants are different both chemically

and by weight percentage and produce unique fracture resistance. When this fracture toughness and energy are plotted with respect to weight percentage, an interesting trend is observed as shown in Figure 1. There exists a binder wt.% where the fracture toughness is maximized and the fracture energy is minimized. This trend may not be true due to the different materials used in the PBXs. The motivation of this study is to determine if a similar trend can be observed in a PBX composed of the same materials at different binder wt.%.

Strain field distribution on PBX simulants, in particular near notch tip for different compositions has been analyzed to evaluate deformation pattern by Digital image correlation (DIC) method. It is a non-contact displacement measurement technique [4]. Quantitative and qualitative studies on the fracture behavior of PBX have been performed using DIC. The DIC method is applied as a real-time tool to locate the site of crack initiation and, track propagation to rupture [9]. It has been applied to calculate the thermal expansion and Poisson's ratio [12]. It can be quantitatively applied to record strain using virtual strain gauges depicted as contours, isolines, and/or vectors [12], [13]. Micro and SEM-based DIC have been employed to study the dynamic micro-cracking process at the binder-particle interfaces [14]. Three-dimensional DIC has been employed to measure the out of plane displacement in cylindrical PBX specimen [16]. The DIC method has been applied to study the shock sensitivity of PBX at high strain rates [17], [18]. Studies using DIC have shown that the ASTM standard E1820 for fracture toughness of metallic materials is suitable for obtaining a homogenized description of fracture in PBXs [9]; however, further investigation into the fracture energy, G_f metric for PBXs need to be performed.

In this study, the fracture behavior and resistance of a polymer bonded explosive will be reported. An 80 wt.% soda lime glass and 20 wt.% high impact polystyrene PBX simulant is manufactured and subjected to indirect tensile and compression tests to establish the credibility of the simulant. The semi-circular bending (SCB) test is applied to measure the fracture toughness and energy. This process is repeated for other three different compositions of PBX simulant that includes different notch dimension and manufacturing temperature. Statistical analysis of the two fracture resistance metrics is performed. Three-dimensional digital image correlation (3D-DIC) is

performed to analyze the fracture behavior of the PBX simulant. Micrographs from a scanning electron microscope (SEM) are investigated to evaluate the bonding of the particle polymer interface, as well as the ductile and brittle nature of fracture and dissemination of crack path.

Material and Test Method

Material and Manufacturing

The PBX simulant in this study is composed of spherical soda lime glass beads (SLGB) and Polystyrene 825 [29]. The soda lime glass beads (SLGB) offers a high modulus contrast between the particle and binder plasticizer. The SLGB were manufactured by Jaygo Corp with an average diameter of 200 μm±50μm, the density of 1.02 g-cm-3, the elastic modulus of 63 GPa, and Poisson's ratio of 0.20. The average diameter is within the range of the real energetic Pentaerythritol tetranitrate (PETN) at 44-850 μm.

High Impact Polystyrene (HIPS) 825 is selected as the binder material because it is a classic and common binder employed in real PBX compositions [19]. The HIPS pellets were manufactured by Total Petrochemicals & Refining USA Inc. The Vicat softening and auto-ignition temperature of the HIPS is 205 and 440°C respectively with a melt flow at 94°C-5 kg of 8.0 g per 10 min. The product at room temperature has a density of 1.04 g-cm-3, elastic modulus of 2.275 GPa, the tensile strength of 24.821 MPa, and Poisson's ratio of 0.35.

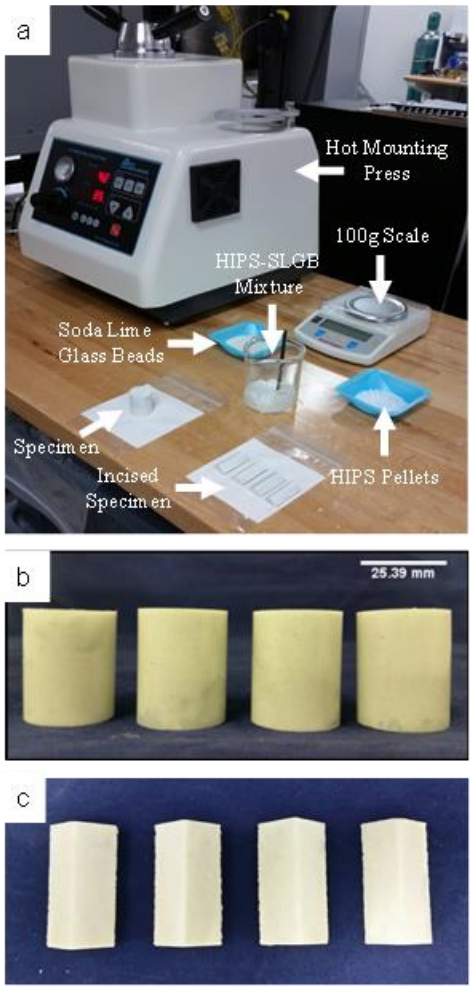

Figure 2 – Specimen preparation (a) manufacturing setup (b) product (c) incised view

The PBX simulants are composed of varying weight percentages ranging from 80 wt% SLGB and 20 wt% HIPS to 83 wt% SLGB and 17 wt% HIPS. The manufacturing setup is depicted in Figure 2(a). The PBX simulant is prepared according to a newly established method [20]. A mixing beaker and stirring rod are used to prepare an initial mixture of PBX simulant constituents. The SLGB is poured into the beaker and 0.5 mL of distilled water is added and mixed until the SLGB beads are well coated. The HIPS is added to the beaker and the mixture is stirred for 2 minutes. Water helps to induce a strong particle agglomeration effect where the SLGB binds to the HIPS pellets.

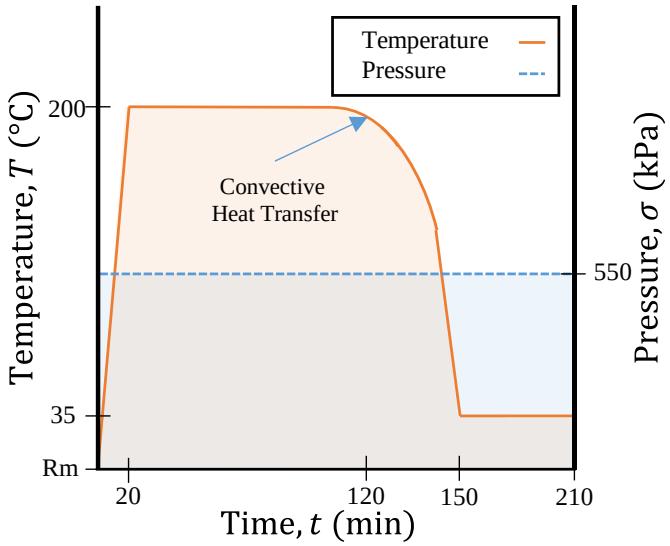

Figure 3 – Temperature, Pressure, and Time Process of Manufacture

The PBX simulant is pressured together using a hot pneumatic mounting press with a 25.4 mm mount. A temperature, pressure, and time manufacturing process plot is provided in Figure 3. Pressure is held at 550 kPa throughout compaction. The temperature is raised from room temperature to 200°C in 20 min and then held at 200°C for 100 minutes. The specimen is cooled using a water circulation tank for 30 minutes or until a temperature of 35°C is achieved. The pressure is held for an additional 60 min at 35°C before the manufacturing process is completed. The product is a 25.4 mm diameter and 34.3 mm length cylinder as shown in Figure 2(b). A symmetrically bisected specimen demonstrates the internal structure is visual defects free as shown in Figure 2(c).

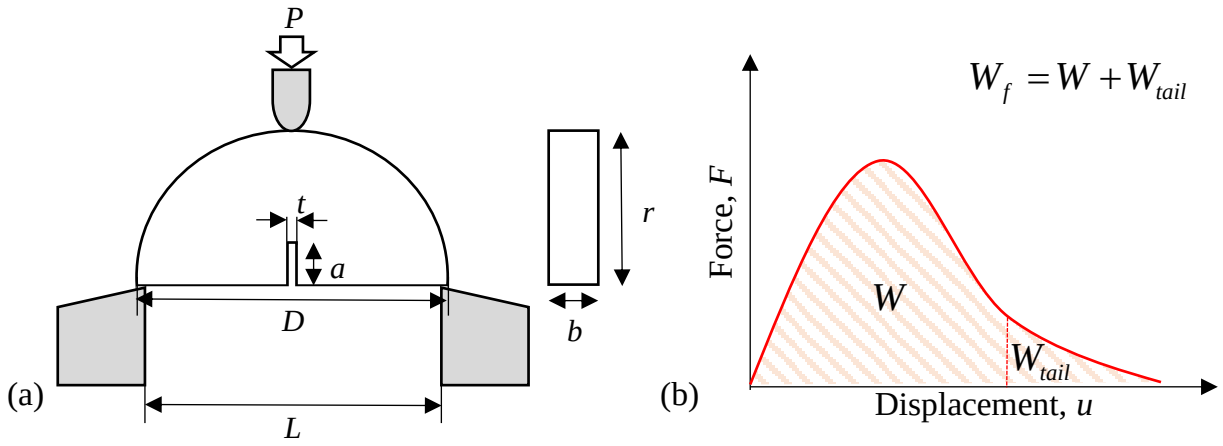

Figure 4 – Semi-circular bending test (a) setup (b) strain energy measurement

Table 2 – Specimen dimensions

Diameter, D (mm)	Thickness, b (mm)	Notch Depth, a (mm)	Notch Thickness, t (mm)	Notch Depth to Radius, a/r
25.4	12.7	1.0	0.2	0.079

Semi-Circular Bending Test (SCB)

The SCB specimens are machined using a computer numerical control (CNC) machine. The dimensions are provided in Table 2. The SCB tests are conducted using an ADMET expert 5603 Table-Top universal test system with an MTESTQuattro controller. This electromechanical frame is equipped with a ±4.5kN load cell. During the test, the specimen is mounted in a three-point bend fixture and subjected to compression as illustrated in Figure 4(a) according to the AASHTO TP 105-13 standard [42]. Teflon tape and lubricate is applied to the compression platens to minimize friction. The distance between the support anvils, L is 23.4mm. The diameter of the load and support anvils is 5 mm. An initial seating load of 80 N is imposed on the specimen. The SCB tests are executed under displacement control at a rate of 0.5 mm/min.

Fracture energy, G_f is calculated using the single-specimen geometry-specific solution of the critical strain energy release rate, J_c or a three-point bending specimen proposed by Rice [29].

The fracture energy is obtained by dividing the work of fracture, W_f the total area under the load vs. load line displacement curve depicted in Figure 4(b) by the ligament area, A_{lig} as follows

$$G_f = \frac{W_f}{A_{lig}}, \quad A_{lig} = (r-a)b; \tag{1}$$

where, G_f is the fracture energy (kJ-m-2), W_f is the work of fracture (J), A_{lig} is the ligament area (mm2), r is the specimen's radius (mm), a is the notch depth (mm), and b is the specimen thickness (mm). It should be noted that a unit conversion is needed to calculate G_f using the given units.

The work of fracture, W_f can be partitioned as follows

$$W_f = W + W_{tail} \tag{2}$$

where, W is the strain energy obtained from the area under the experimental load-displacement curve and W_{tail} is the area under an extrapolated continuation/tail of the curve to zero. The experimental strain energy, W is calculated using the quadrangle rule [25]

$$W = AREA = \sum_{i=1}^{n} (u_{i+1} - u_i) \cdot (P_i) + \frac{1}{2} \cdot (u_{i+1} - u_i) \cdot (P_{i+1} - P_i) \tag{3}$$

where P_i is the applied load and u_i is the load line displacement at the i step, and P_{i+1} is the applied load and u_{i+1} is load line displacement at the $i+1$ step. The extrapolated strain energy, W_{tail} is calculated by fitting a power law to the load-displacement curve as follows

$$P = \frac{c}{u^2} \tag{4}$$

This function is only valid for the portion of the post-peak load-displacement curve below 60% of the peak. The extrapolated strain energy W_{tail} is calculated as

$$W_{tail} = \int_{u_c}^{\infty} P du = \int_{u_c}^{\infty} \frac{c}{u^2} du = \frac{c}{u_c} \tag{5}$$

where, u_c is the load line displacement value at which the test is stopped.

Fracture toughness, K_{Ic} is defined as the stress intensity factor corresponding to the initiation of the crack. The stress intensity factor should be computed as follows

$$K_{Ic} = Y_{I(0.8)} \sigma_0 \sqrt{\pi a} \tag{6}$$

where is the dimensionless geometric factor, σ_0 is the applied stress, and a is the notch depth [24], [26]. The applied stress is calculated as $\sigma_0 = P_{\max}/2rt$ where $P_{\max}$ is the peak load, and r and t are the specimen radius and specimen thickness respectively. The dimensionless geometric factor, $Y_{I(0.8)}$ is calculated [26] as follows

$$Y_{I(0.8)} = 4.782 + 1.219\left(\frac{a}{r}\right) + 0.063\exp\left[7.045\left(\frac{a}{r}\right)\right] \tag{7}$$

where a is the notch depth (mm) and r is the specimen's radius (mm).

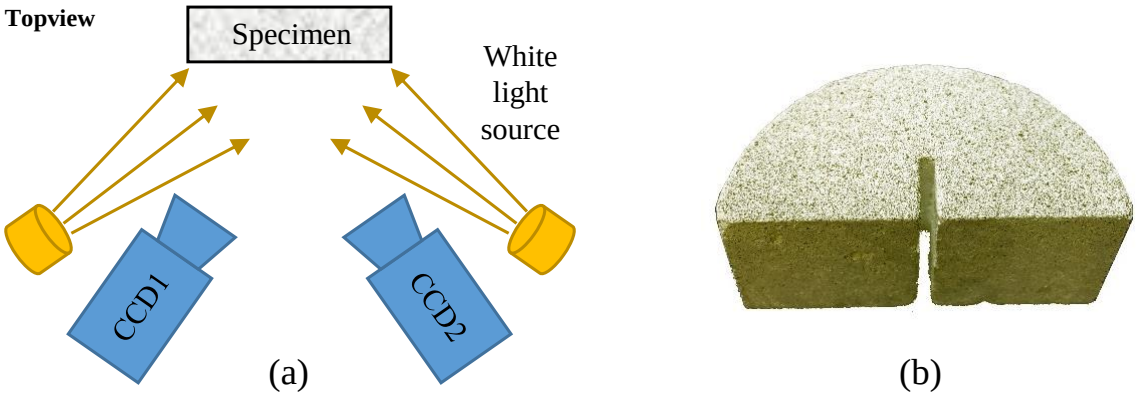

Figure 5 – Digital image correlation (a) 3D setup and (b) speckled specimen with exaggerated notch

3D Digital Image Correlation

In this study, the Correlated Solutions VIC-3D digital image correlation hardware and software package is employed. An illustration of the 3D-DIC setup is provided in Figure 5(a). Two charge-coupled devices (CCD) cameras and 1500 Lumen LED white lights are focused on the specimen-testing zone. Photos of a calibration square are taken to provide a physical reference of pixel distances. Specimens are primed with a random speckle pattern as shown in Figure 5(b). The speckles act as physical reference points. The VIC-3D system and AMDET 5603 test machine are synchronized such that the ADMET load and VIC-3D displacement are at the same frequency. The 3D DIC software tracks the displacement of speckled reference points compares the displacements to the calibrated physical reference and calculates strain using the axioms of continuum mechanics. After testing, the images taken from 3D DIC are used to investigate the

crack path, its evaluation with time and nature. The crack length is measured using an image processing and analysis software, Image J.

Results and Discussion

Tensile and Compressive Properties

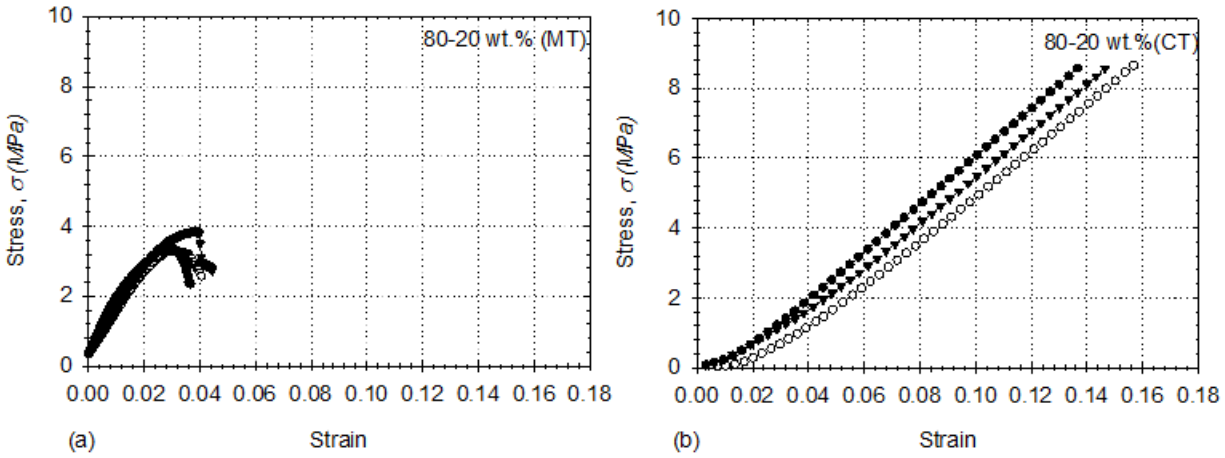

Figure 6 – Stress-Strain Response of PBX simulant (80-10 wt.%) in (a) indirect tension and (b) compression

The tensile properties of the 80-20 wt.% PBX simulant are collected using indirect tensile (IDT) and compression tests based on ASTM D6931 and D695 respectively [21], [22]. The average ultimate tensile strength (UTS) of the PBX simulant is measured 3.387±0.5 MPa. Young's modulus of the indirect tensile test is calculated as 128.6 MPa. Despite the wide range of variability in mechanical properties of explosive materials, this 80-20 wt.% PBX simulant's ultimate tensile strength is aligned with PBX 9404 [41]. While specimens are undergoing the tensile tests, the specimens break apart comparatively quicker than compressive test as shown in Figure 6. It is observed that the specimens undergo extensive plastic deformation for compressive test and failure is ductile in nature. The IDT response of the PBX simulant is uniform in the elastic regime but varies once the material transitions into the plastic regime. The MT1, MT2, and MT3 tests are observed to harden non-linearly followed by a load drop that is arrested by a perfectly plastic response. This drop is likely due to a local weak-zone (perhaps a pileup of weakly bonded SLGBs) where the particle-matrix interface breaks. The stiffness of the material is recovered via stress redistribution. In the IDT specimens, the crack initiates along the center of the specimens and

propagates vertically toward the outer radius. In the cases involving a load drop, the primary crack bifurcates and secondary cracking initiates along the crack path.

Fracture Resistance

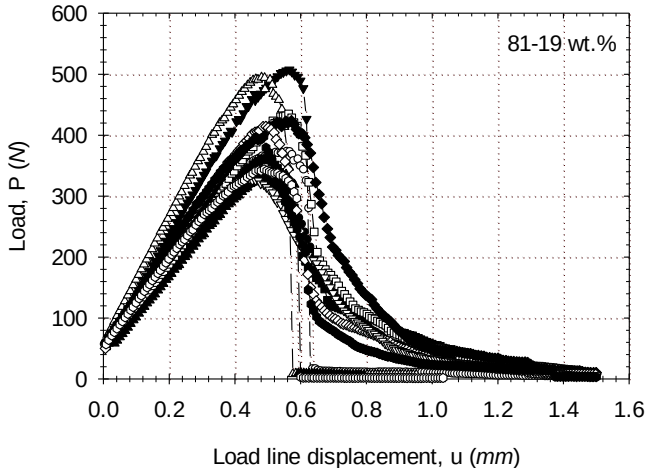

Figure 7– Load-displacement curve for PBX with a brittle and ductile failure

At all compositions, both brittle and ductile fracture was observed. The reason for this random behavior is due to how the HIPS binder and SLGB particulate adhere during manufacturing. Example of this phenomena is depicted in Figure 7. Both the brittle and ductile fracturing specimens exhibit linear elastic regions; however, the brittle specimens have a higher slope at the load and displacement curve that indicates higher modulus of elasticity but less plasticity. The brittle specimens reached an average peak load of 417.12 N and fractured because they are unable to continue to carry the load while the ductile specimen reach an average peak load of 385.99 N and gradually soften carrying the load for a considerable amount of displacement. Among twelve 81-19 wt.% of PBX simulant semi-circular bending test, 28 percent are found brittle in nature and rest of 72 percent tests are found as ductile in nature. Ductile behaviors are prevailed because of the quantity and nature of polymer binder exists at 81-19 wt.% of PBX simulant. This brittle/ductile fracture issue is further described in section Fractography.

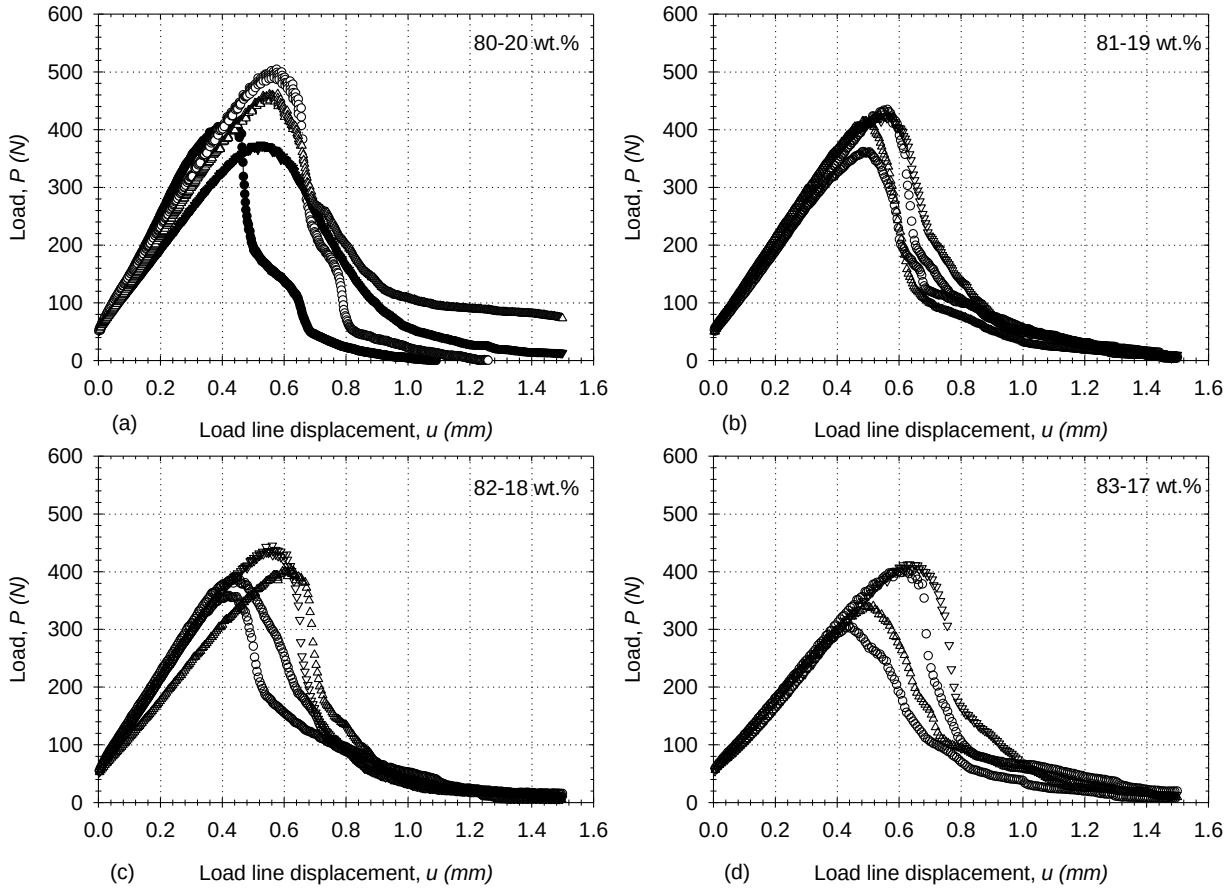

Figure 8 – Load-displacement curve for PBX simulant at (a) 80-20, (b) 81-19, (c) 82-18, and (d) 83-17 wt.% compositions

To analyze the fracture energy with respect to composition, the ductile behavior fracture test results were compared. SCB tests were run for each weight percentage that was manufactured. The load and displacement curves are shown in Figure 8. An average maximum load of 326, 401, 411, and 408 N are measured for the 83-17, 82-18, 81-19, and 80-20 wt.% specimens respectively. The fracture energies are calculated for them to be 1.373, 1.504, 1.482, and 1.954 kJ/m2 respectively. The coefficient of variation (COV) for fracture energy is also calculated for each weight percentage. For 83-17, 82-18, 81-19, and 80-20 wt.% composition, the coefficient of variation of fracture energy are 30, 10, 8, and 26% respectively. This data is more elaborately stated in Table 3 to Table 6.

Table 3 – Fracture resistance of the 80-20 wt.% specimens

Specimen Name	Notch Depth, a *(mm)*	Peak Load, P_{max} *(N)*	Work of Fracture, W_f *(J)*	Fracture Energy, G_f *(kJ/m^2)*	Fracture Toughness, K_{Ic} *($MPa\text{-}m^{0.5}$)*
SN 1	0.770	464.33	0.304	2.139	0.374
SN 2	0.750	480.06	0.225	1.604	0.388
SN 3	0.630	499.71	0.190	1.271	0.348
SN 4	0.820	504.32	0.251	1.642	0.389
Average	0.743	487.11	0.243	1.664	0.375
St. Dev.	0.081	18.47	0.048	0.358	0.019
COV %	11%	4%	20%	22%	5%

Table 4 – Fracture resistance of the 81-19 wt.% specimens

Specimen Name	Notch Depth, a *(mm)*	Peak Load, P_{max} *(N)*	Work of Fracture, W_f *(J)*	Fracture Energy, G_f *(kJ/m^2)*	Fracture Toughness, K_{Ic} *($MPa\text{-}m^{0.5}$)*
SN 1	0.919	362.61	0.200	1.413	0.318
SN 2	0.896	440.54	0.222	1.465	0.357
SN 3	0.802	424.75	0.243	1.657	0.337
SN 4	0.803	416.69	0.201	1.392	0.336
Average	0.855	411.148	0.216	1.482	0.337
St. Dev.	0.061	33.844	0.020	0.121	0.016
COV %	7%	8%	9%	8%	5%

Table 5 – Fracture resistance of the 82-18 wt.% specimens

Specimen Name	Notch Depth, a *(mm)*	Peak Load, P_{max} *(N)*	Work of Fracture, W_f *(J)*	Fracture Energy, G_f *(kJ/m^2)*	Fracture Toughness, K_{Ic} *($MPa\text{-}m^{0.5}$)*
SN 1	0.613	359.01	0.185	1.282	0.256
SN 2	0.433	393.04	0.216	1.550	0.246
SN 3	0.660	446.37	0.227	1.608	0.337
SN 4	0.558	406.79	0.221	1.574	0.285
Average	0.566	401.304	0.212	1.504	0.281
St. Dev.	0.098	36.140	0.019	0.150	0.041
COV %	17%	9%	9%	10%	14%

Table 6 – Fracture resistance of the 83-17 wt.% specimens

Specimen Name	Notch Depth, a *(mm)*	Peak Load, P_{max} *(N)*	Work of Fracture, W_f *(J)*	Fracture Energy, G_f *(kJ/m^2)*	Fracture Toughness, K_{Ic} *($MPa\text{-}m^{0.5}$)*
SN 1	0.720	407.07	0.235	1.642	0.316
SN 2	0.789	305.74	0.166	1.272	0.271
SN 3	0.798	420.89	0.246	1.697	0.338
SN 4	1.143	340.99	0.194	1.414	0.339
Average	0.863	368.672	0.210	1.506	0.316
St. Dev.	0.190	54.550	0.037	0.199	0.032
COV %	22%	15%	18%	13%	10%

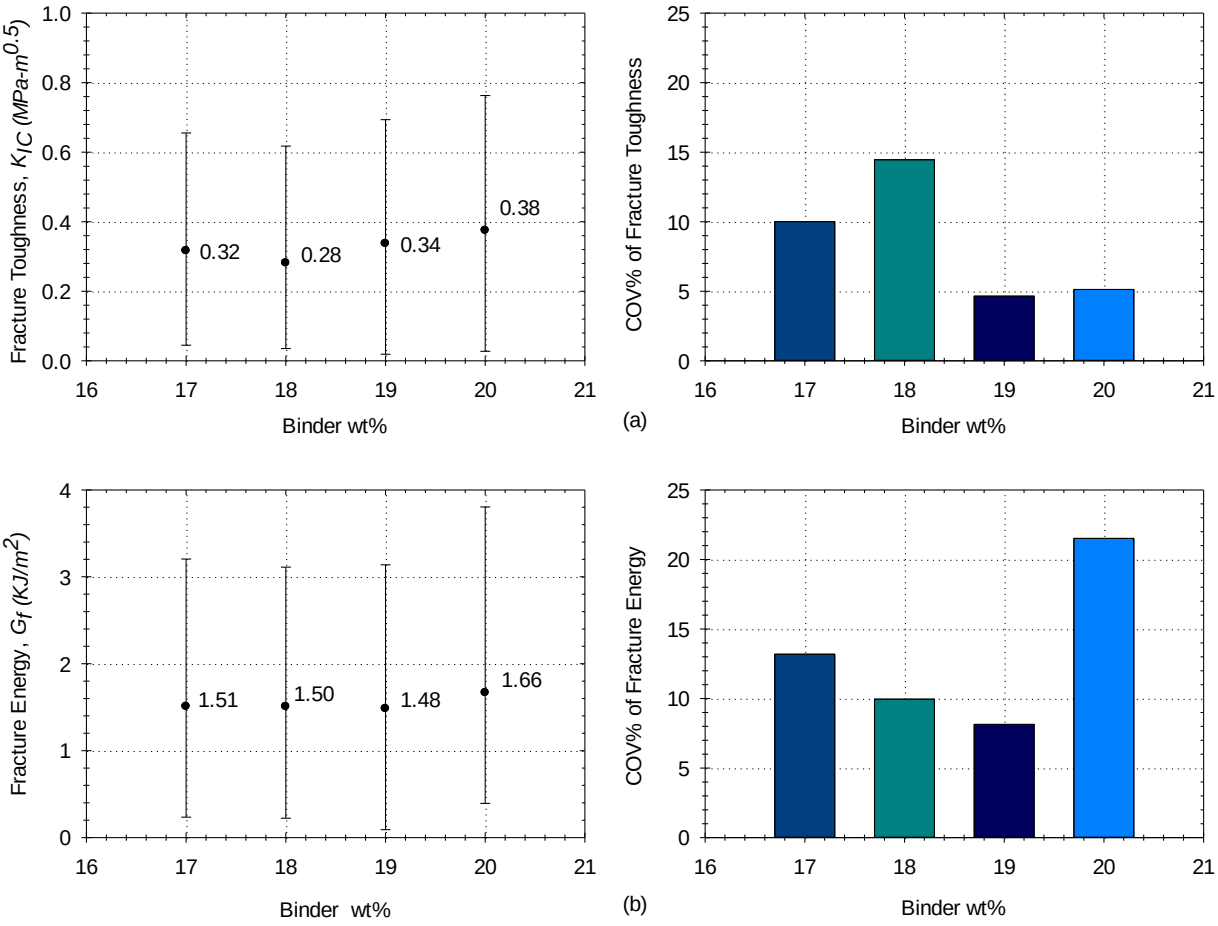

Figure 9 – Fracture resistance and corresponding COV of PBX simulant with respect to binder wt.%: (a) Fracture Toughness and (b) Fracture Energy

It is observed that as the weight percentage of the SLGB decreases and the weight percentage of the Polystyrene pellets increases, the coefficient of variation for both fracture toughness and energy decrease as shown in Figure 9. Also, as the HIPS weight percentage is increased, the fracture toughness and strain energy release rate are increased. This is because the HIPS binder reduces the number of voids that may occur at various matrices the SLGB have during manufacturing. This nature of alteration dominates PBX simulants ductile failure behavior.

Digital Image Correlation

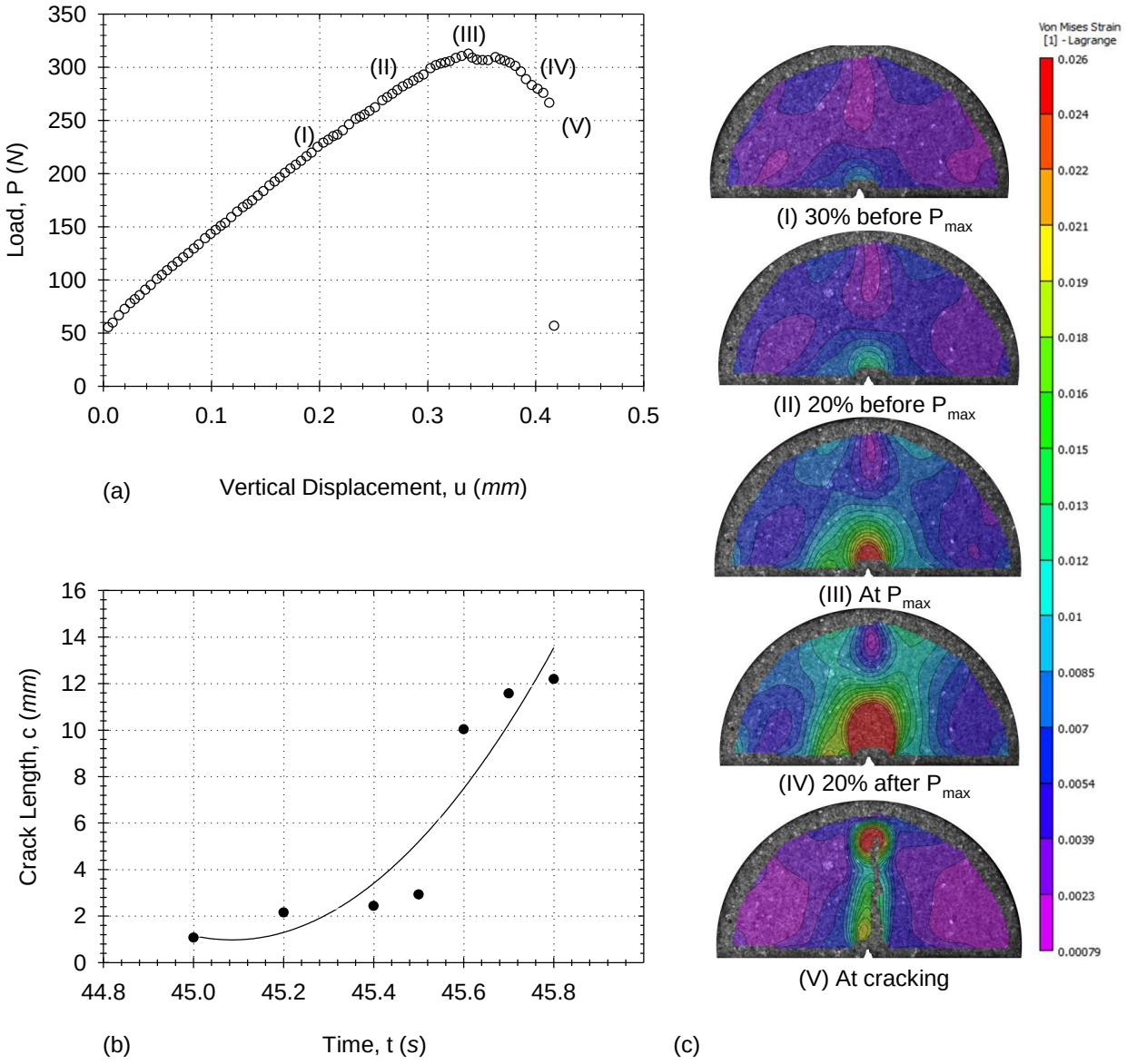

Figure 10 – (a) Load-displacement curve corresponding to von Mises strain (b) crack propagation with time and (c) von Mises strain contours for an 80-20% composition

The 3D DIC system identified the primary crack initiation site, crack propagation path and strain fields of the PBX simulant as shown in Figure 10. Using the DIC system, contours of the von Mises strain are plotted over the specimen as shown in Figure 10(c). The von Mises strain is calculated as follows

$$\varepsilon_{vm} = \frac{1}{1+\nu'}\sqrt{\frac{1}{2}\left[\left(\varepsilon_1-\varepsilon_2\right)^2+\left(\varepsilon_2-\varepsilon_3\right)^2+\left(\varepsilon_3-\varepsilon_1\right)^2\right]} \tag{8}$$

$$\nu' = -\frac{\varepsilon_T}{\varepsilon_L}$$

where $\varepsilon_1, \varepsilon_2$ and ε_3 are the 1st, 2nd, and 3rd principal strains, ε_T and ε_L are the transverse and longitudinal strains, and ν' is the instantaneous Poisson's ratio. At 80% of peak load (I), a small strain concentration is observed at the notch. As the load increases, the strain concentration increases in size and intensity. At the peak load (III), ε_{vm} is maximized at 0.026. Low-intensity strain concentrations appear on the outer radius of the specimen to the left and right of the load anvil. From the peak load (III) to post-peak load (IV), the size of the strain concentration increase suggesting the growth of the plastic zone. Between (IV) and (V), the critical strain energy release rate is exceeded and fracture occurs as indicated by the rapid extension of the crack.

Overall, the PBX simulant behaved like a homogeneous material. The heterogeneous microstructure and defects did not produce extra strain concentrations visible on the surface of the specimen. Upon fracture, the crack propagated from the notch tip and took a tortuous vertical path through the material. These findings help support the narrative that the manufacturing process in this study produces a credible PBX simulant.

Fractography

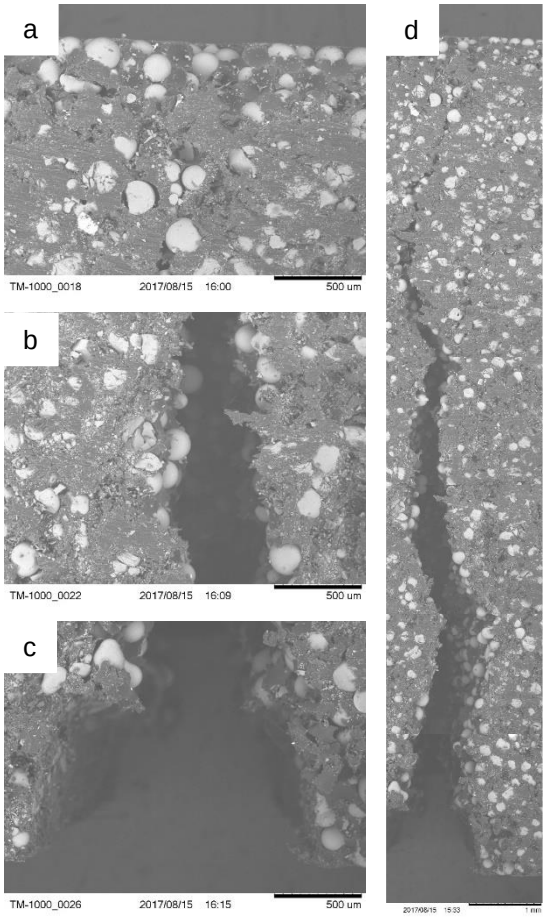

Figure 11 – Micrograph of SCB specimen (a) notch tip, (b) mid-section, (c) top section, and (d) complete crack path

Scanning Electron Microscope was applied to analyze the crack propagation and the micromechanics of the failed specimens. An image of the notch tip was taken in order to observe the SLGB and HIPS matrix as shown in Figure 11(c). While there was usually a higher concentration of SLGB to HIPS, there was no major effect on crack initiation and crack propagation. SEM images of the crack path at midsection and notch tip are shown in Figure 11(b) and Figure 11(a) respectively. It is observed that cracking within the specimens occurred primarily in the HIPS binder due to the lack of fractured SLGB. Each specimen demonstrated cracking in a tortuous manner that was initiated by the prefabricated notch shown in Figure 11(d).

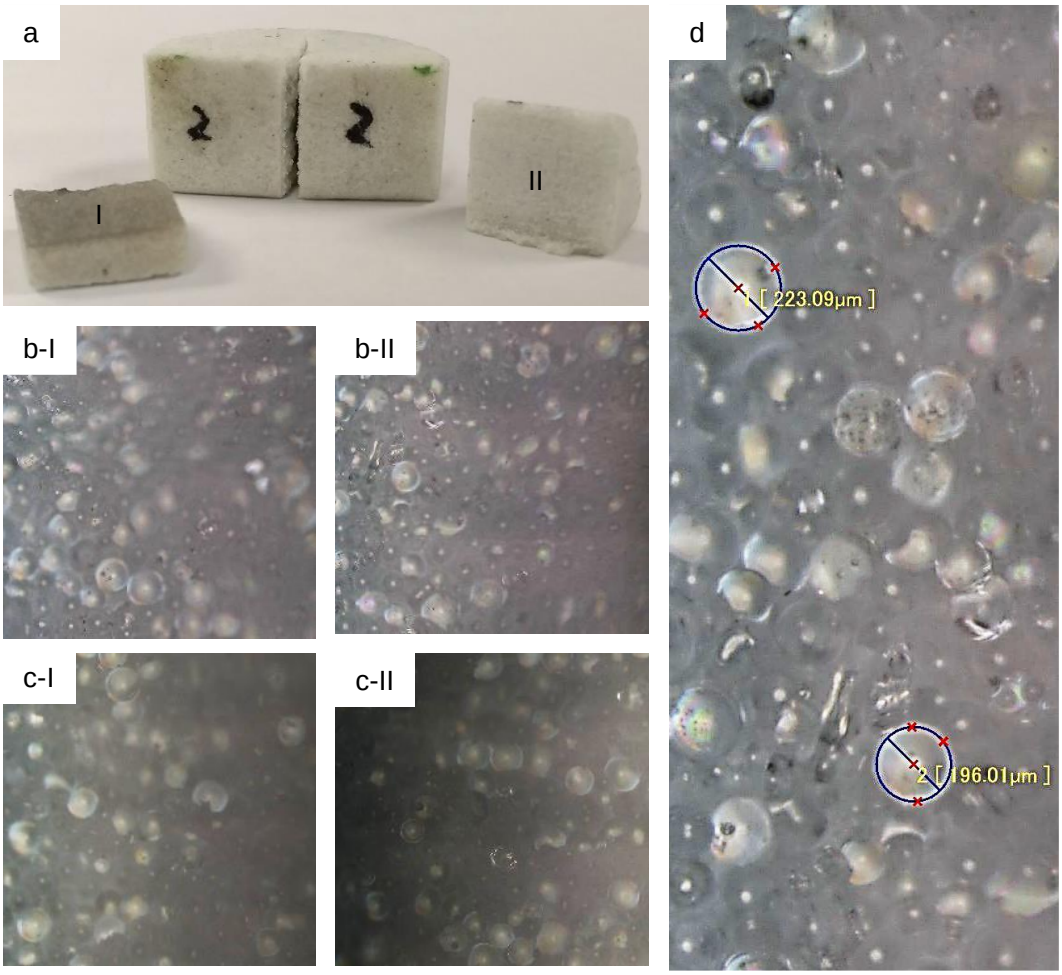

Figure 12 – (a) PBX Simulant after testing, (b) Brittle fracture of face I and II at 1000x1000 pixel, (c) Ductile fracture of face I and II at 1000 x 1000 pixel, (d) Measurement of SLGB of fracture surface

Micrograph of the fracture surface of ductile and brittle material taken by KEYENCE VHX 5000 digital microscope are shown in Figure 12. The higher density of SLGB particle is found in brittle materials. The diameter of SLGBs are calculated using built-in feature of that microscope. The average diameter is found $200 \pm 20\ \mu m$. Total number of SLGB on the fracture surface of the ductile and brittle material is counted for 1000 x 1000 pixel image to compare between them. SLGB particles are sparsely distributed over brittle fracture surface whereas the spatial distribution of SLGBs are found all over the fracture space.

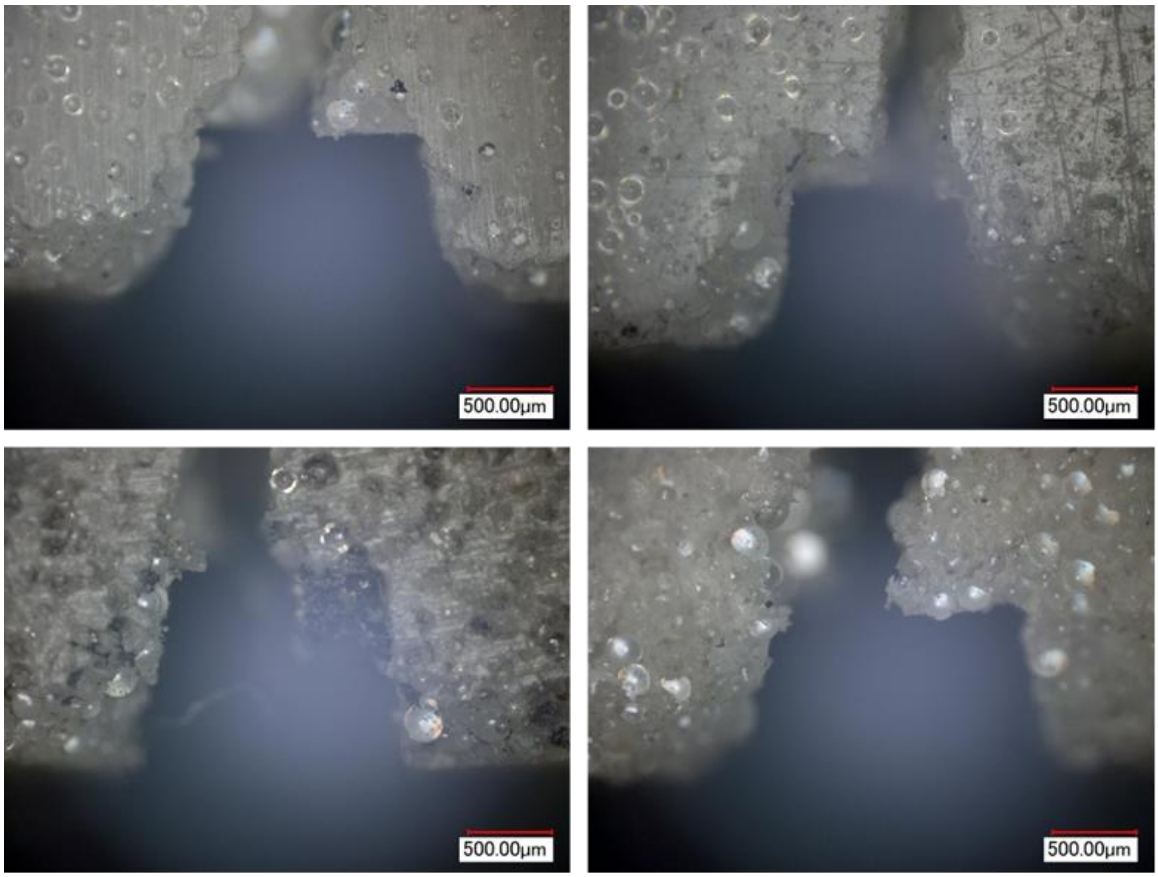

Figure 13 – Notch disconformity of 80-20 wt.% PBX simulant

In all cases, there is no occurrence of bifurcation. It is observed that fracture occurs due to a pullout of the glass bead particles from the polymer binder as depicted in Figure 16. Various machine notch defects due to cutting polymer composite with high-speed CNC machine are observed. Since HIPS has low strength than SLGB, binder material near the notch edge is encountered more deformation. SLGB are displaced and small concave cavities are noticed for pulling out the SLGB particles. Due to this disconformity at machine notch edge, crack initiation is originated from different part of notch section for the different notch.

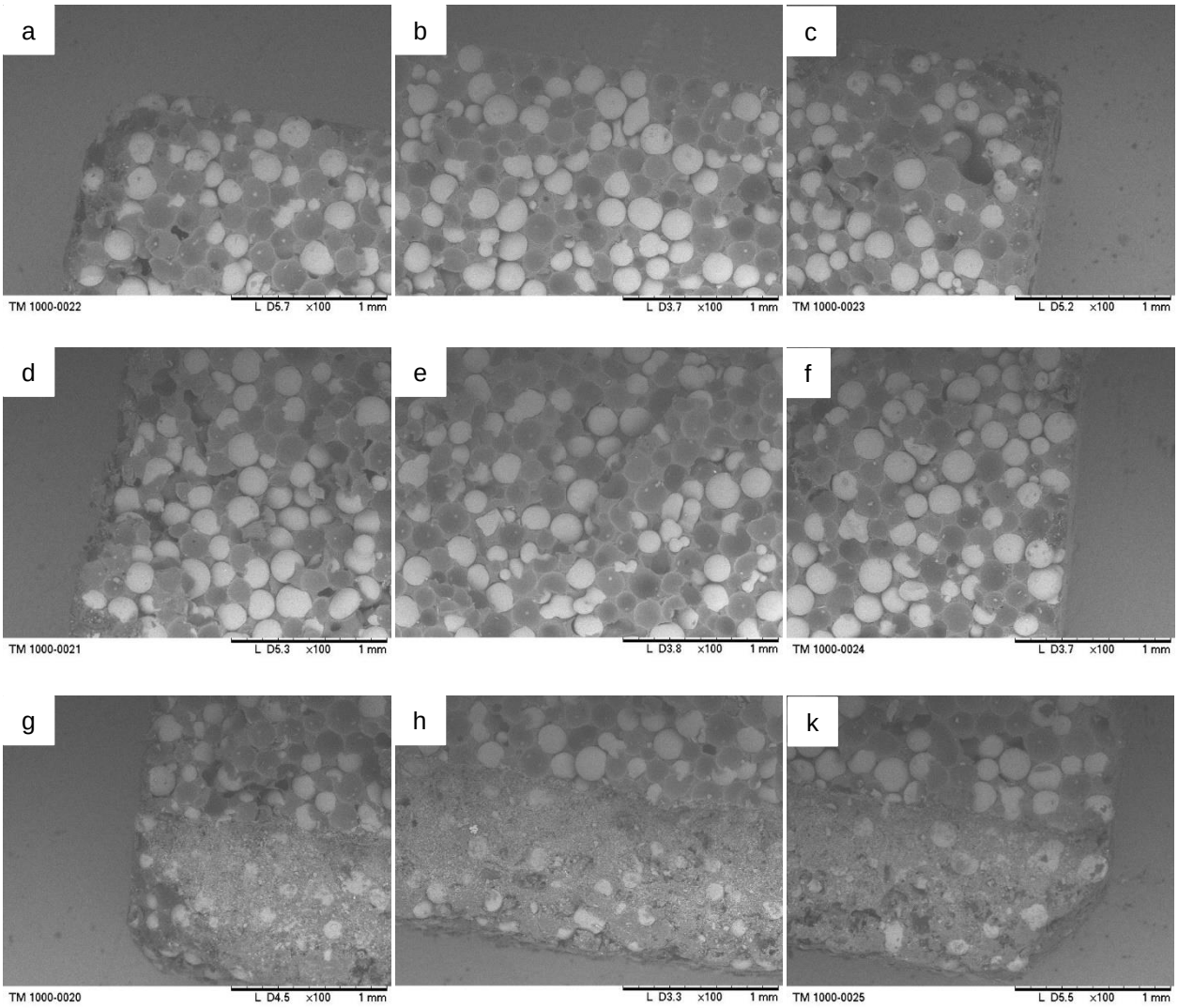

Figure 14 – SEM micrographs of ductile specimen at various locations of fracture surface, (a) Top left, (b)Top center (c) Top right, (d) Mid left, (e) Mid center, (f) Mid right, (g) Notch left, (h) Notch center and (k) Notch right

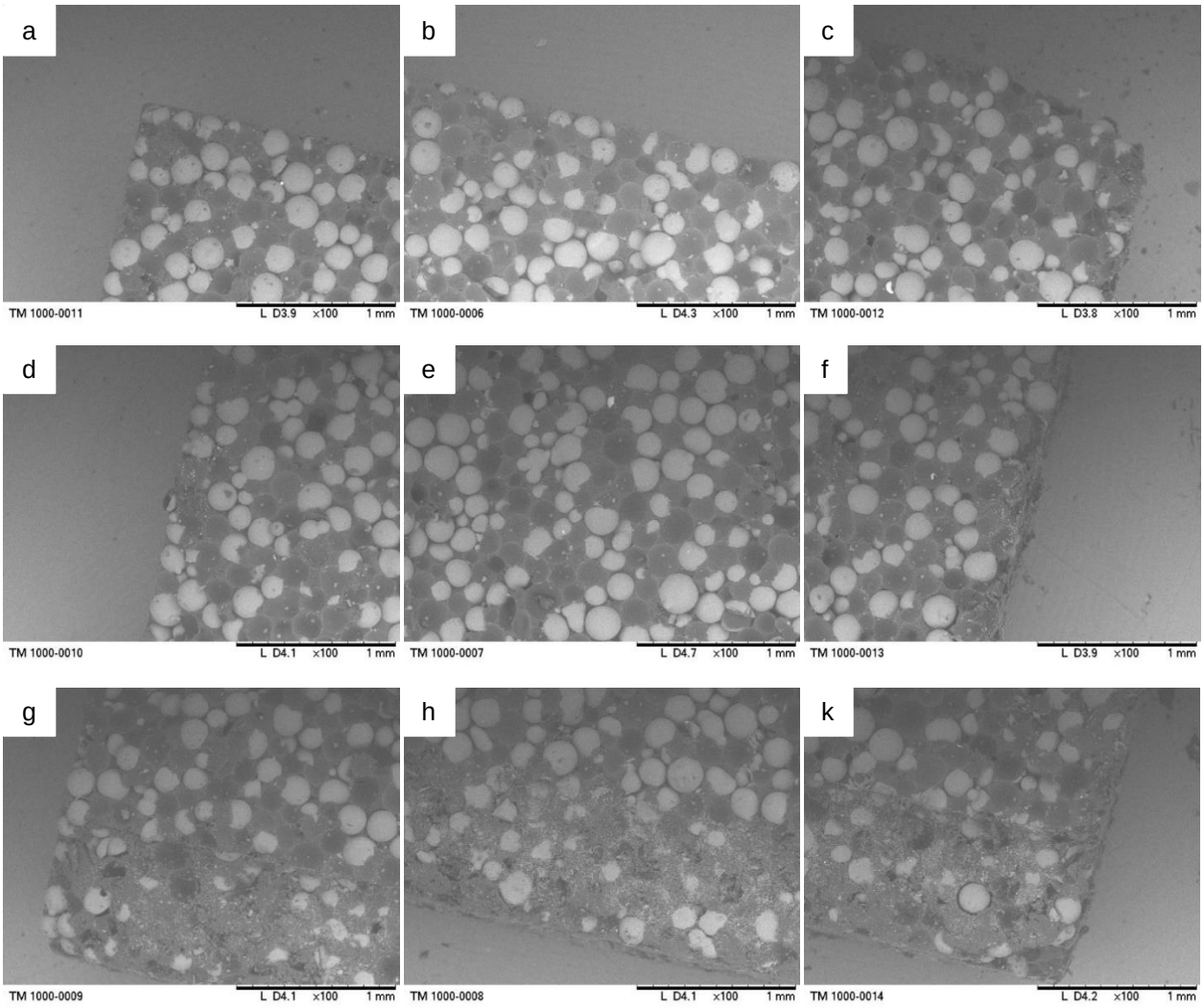

Figure 15 – SEM micrographs of brittle specimen at various locations of fracture surface, (a) Top left, (b)Top center (c) Top right, (d) Mid left, (e) Mid center, (f) Mid right, (g) Notch left, (h) Notch center and (k) Notch right

Evidence of both ductile and brittle behaviors within various specimens are observed in Figure 14 and Figure 15. Throughout the different polymer to particle matrices, the ductile specimens appeared to have a deeper concavity from the pullout of the SLGB when compared to the brittle behavior. Another reason for the ductile and brittle behavior are the differences in the polymer to particulate matrices along the notches of each specimen. The ductile specimens have a higher concentration of polymer along the surface of the notch whereas the brittle specimens have a higher concentration of beads along the notch. The reason for this behavior is due to the how the

specimens were manufactured. As there are higher concentrations of glass beads within an area, there are voids within the polymer-particle matrix which allow the crack to propagate.

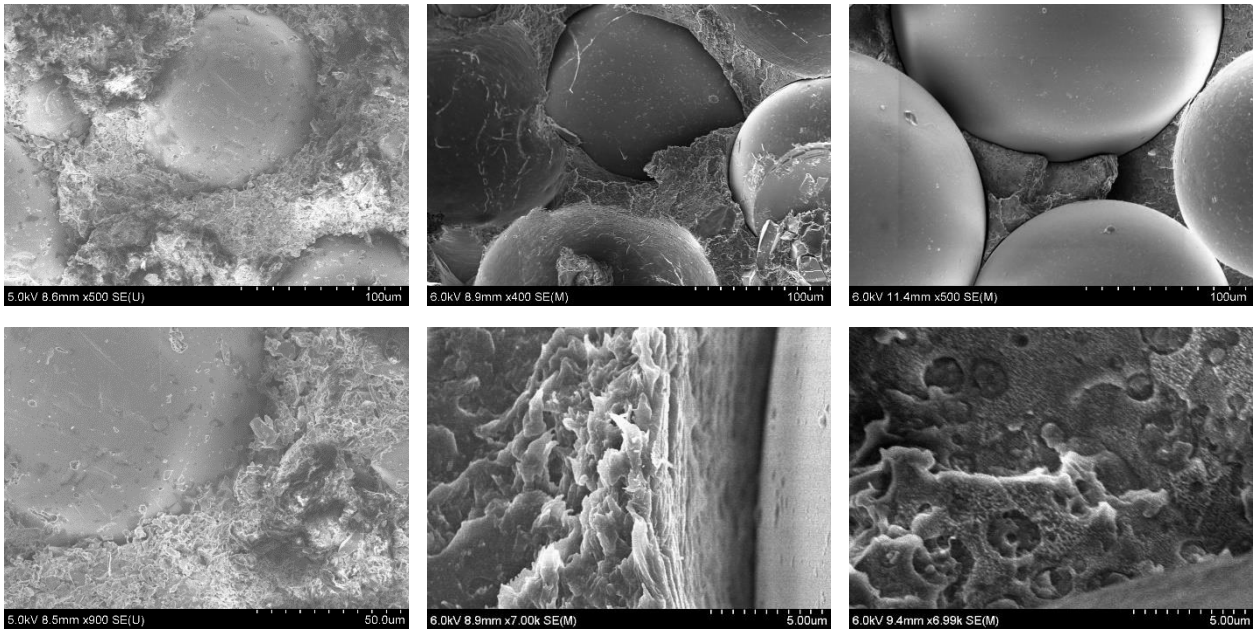

(a) (b) (c)

Figure 16 – SEM image of a specimen (a) machined surface before fracture, (b) ductile surface and (c) brittle surface after fracture

Before conducting mechanical testing on the specimens, SEM images of the surface of the material were taken to observe any microstructural defects within the material as shown in Figure 16. It should be observed that the surface after machining is disproportional. There are also shattered glass particles within the polymer matrix and the glass beads. Lastly, it is noted that while most of the glass beads are coated within the polystyrene, there are many glass beads that are not fully bonded by the polystyrene. These microstructural defects affect whether the material exhibits ductile or brittle behavior while mechanical load is being applied.

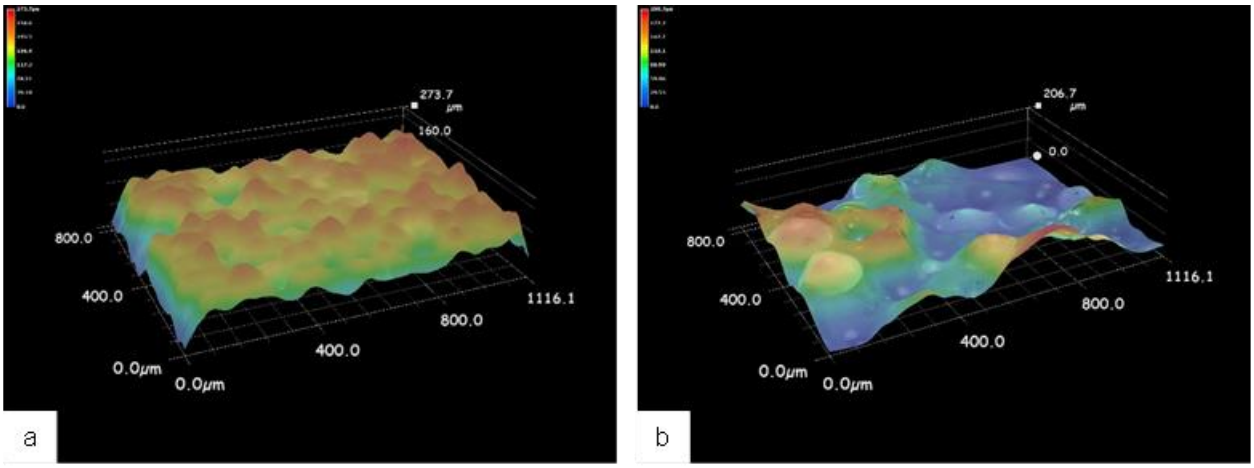

Figure 17 – 3D surfacing image of (a) ductile, and (b) brittle specimen

The ductile and brittle failures of the PBX simulant specimens are further studied using stereo microscopy. Figure 17(a) depicts a 3-D surfacing image of the microstructure of a specimen which experienced ductile behavior and Figure 17 (b) illustrates a 3-D surfacing image of brittle behavior. In the ductile material, as load continued to be applied, there was a higher resistance to cracking due to the SLGB being better coated with the HIPS as load was being applied to the brittle specimens, the crack had little resistance due to some of the glass beads not being fully coated in the polystyrene. This allowed for the crack path to pass around the glass beads and cause instantaneous failure.

Discussion

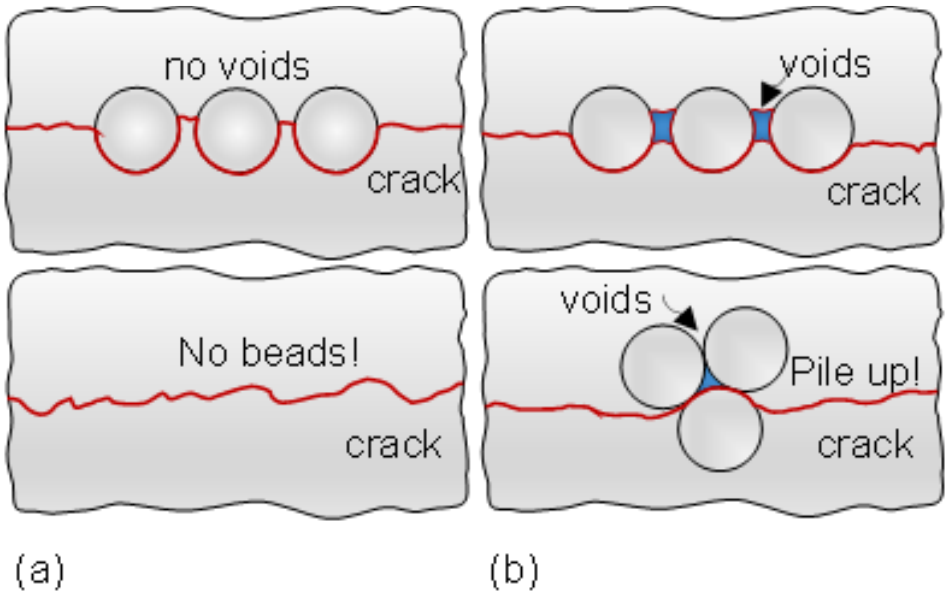

Illustration 1 – Depiction of crack path (a) in ductile and (b) brittle materials

During the tests that were run on the specimens with varying weight percentages, the materials either exhibited a ductile or brittle material. Upon further analysis, it was observed using a digital microscope and a SEM microscope that the specimens that contained a higher concentration of glass beads throughout the crack path experienced brittle mechanical failure and instantaneous cracking whereas specimens that had a higher concentration of polymer near the notch experienced the ductile behavior and a higher resistance to fracture. The brittle behavior is caused by the polymer not being able to flow through the glass beads during the manufacturing process which causes many voids within specimens shown in Illustration 1. Once load is applied, these specimens obtain maximum stress before fracturing. The specimens that have a higher polymer concentration obtained a maximum stress before initial cracking. It should also be noted that as the weight percentage of polymer to glass beads increases the coefficient of variation also increases.

Conclusion

This study was performed to evaluate the mechanical properties of a mock PBX specimen at weight percentages. Additionally, the DIC technique was implemented to surrogate the results obtained from the experimental data. The analysis performed using DIC technique satisfactorily showed the Von Mises strain on of the testing configurations, the prediction of the initiation and propagation of the crack by using the strain fields from DIC post processing. The DIC technique has a high impact, as a tool, in the analysis of heterogeneous particulate composites. The mechanical properties at each testing configurations where extracted and analyzed. Digital microscopy was applied to analyze the surface of the specimens prior to testing and post testing. Analysis using digital microscopy showed that microstructural defects affected whether the specimens were ductile or brittle due to fracture. When comparing the results to different PBX and PBX simulant formulations, the properties vary in magnitude. The potential source of variability for the miner mock formulation can be categorized as the composition, material, and test related. To conclude, the following potential sources of variability were identified: PBXs are complex composite materials with high heterogeneity and anisotropy behavior. Alternative data analysis methods must be implemented to properly characterize the heterogeneous and anisotropy behavior of PBX.

Future Work

In future work, experiments will be prepared to explore the strain rate (0.001 to 1 s^{-1}) and temperature (ambient to 75°C) effect. There is a need to develop a microstructure-level DIC system to obtain a more accurate and clearer picture of the micromechanics within these materials. An outcome of this novel characterization method will be the development of a CDM-based constitutive model for the prediction of the "batch-to-batch" mechanical behavior of energetic materials. This model will be used to simulate the service conditions of mock polymer bonded explosive (PBX) material including uniaxial and multiaxial states of static and dynamic loading.

Chapter 2: Investigation of Low Temperature Cracking of HMAs using Digital Image Correlation and Infrared Thermography

Low temperature cracking, also known as thermal cracking, is a damaging phenomenon that effects transportation materials subjected to cold weather. Low temperature cracks nucleate between pavement layers and within individual layers (at binder-aggregate interfaces) due to thermal contraction mismatch [43]. Thermal cracks form on the top and/or bottom surface of pavements (on the cold-side) and propagate transversely through the depth of the material [44]. When the ambient temperature of the pavement drops below or equal to a critical temperature, fracture will occur. In a constrained specimen, this critical temperature is correlated to the rise of thermal stresses that when greater than the ultimate tensile strength lead to fracture [45]. Critical temperature can also be correlated to linear elastic fracture mechanics parameters where the stress intensity factor and/or strain energy release rate increase as temperature decreases until the temperature-dependent fracture toughness and/or fracture energy are met [46]. Material, environment, and geometry are all factors that influence thermal cracking [47].

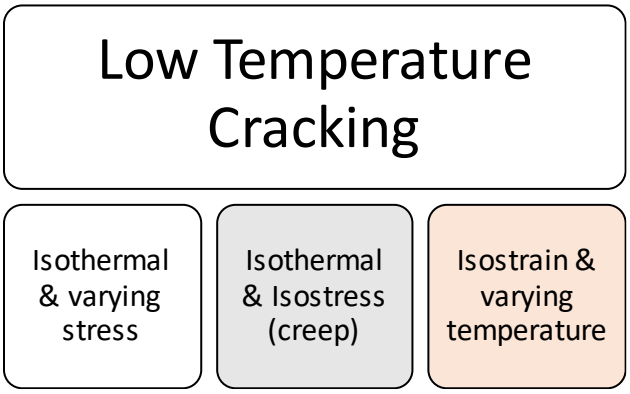

Illustration 2 – Low temperature cracking categories

Low temperature cracking can be characterized into three different test configurations as illustrated in Illustration 2.

In case 1, temperature is fixed (isothermal) and stress is increased to fracture. Fracture is driven by mechanical loads and the measured the fracture resistance (ultimate tensile strength,

fracture toughness, fracture energy, etc.) is specific to the isotherm. Case 1 is the most common configuration for measuring low temperature cracking with test standards established for numerous specimen geometry and load configurations (uniaxial, three- and four-point bending, semi-circular bending test etc.) [54][55].

In case 2, a constant stress is applied to an isothermal temperature. Fracture is driven by the accumulation of inelastic creep strain in the specimen to rupture and specific to the isotherm [43]. In asphalt mixtures, creep is usually characterized using indirect tensile tests (IDT) [99] while in pure asphalt binder it is characterized using the bend bending rheometer (BBR) test [100], [101]. Recently, a provisional standard for the creep of asphalt mixtures in the (BBR) configuration has been developed [54], [102].

In case 3, displacement is fixed at the supports (isostrain) and temperature is lowered until fracture. Fracture is driven the accumulation of thermally induced strains and stresses within the specimen to fracture. The fracture resistance is measured as both the critical temperature and fracture strength (at said temperature) specific to the material [49]; the results of which are ideal for characterizing fracture driven by climate [49][51][56]. The thermal stress restrained specimen test (TSRST) is an established standard that operates under these conditions [103].

The TSRST Test

The TSRST test is widely applied to evaluate the low temperature cracking of asphalt mixtures due to ease of use and the simulation of field conditions [49],[51]. The critical temperature and fracture strength (at said temperature) is dependent on the asphalt type, aggregate type, air void content, size, degree of aging, stress relaxation, and cooling rate [45]. According to Jung and Marasteanu, as the cooling rate is increased, fracture temperature occurs at warmer temperatures [50], [53]. Having a lower cooling rate allows for more stress relaxation which in turn causes fracture at a lower temperature but also a decrease in fracture strength [50]. Fracture strength and fracture temperature are inversely correlated [53]. Thermal contraction occurs in both the aggregate and binder materials. The majority of tensile strain, however, will occur in the binder,

due to the binder having a low modulus [52]. A downside to the TSRST test is it provides a global measure of the fracture resistance only. Information concerning crack nucleation and crack propagation is not recorded. It would be valuable to identify not only the global resistance to low temperature fracture but also the internal local resistance on the surface of specimens. Digital image correlation has the potential to provide this valuable information within the TSRST test protocol.

Digital Image Correlation (DIC)

Digital image correlation (DIC) is an optical non-contact method for measuring the displacement and strain field on the surface of objects. The advantage of DIC over traditional devices such as strain gauges, LVDTs, and extensometers is that DIC provides local information that is not restricted by gauge length but rather resolution (i.e. pixel density) enable measurements ranging from the atomistic to geophysical scale [58]. In DIC, a speckle pattern is applied to the specimen and digital images taken during testing. The speckles act as reference points enabling the relative displacement in the surface of the specimen to be tracked (using a selected cross-correlation criterion) and the displacement gradient and strain calculated according to continuum mechanics [57].

In asphaltic mixtures, DIC has been applied to assess the adequacy of test standards, elucidate the local gradients within material heterogeneities and their contributions to isothermal cracking characteristics, and validate numerical models [59].

In terms of tests standards, Kim and Wen applied DIC to assess the adequacy of LVDT gauge lengths in IDT tests [60]. Stewart et al applied DIC to compare the strain concentrations in two competing fracture resistance standards; the semi-circular bending (SCB) and disk-shaped compact tension (DCT) configurations respectively [61]. Romeo et al applied DIC to extended the asphalt binder SuperPave™DTT geometry to accommodate asphaltic mixtures [62]. Recently, Ramos et al explored how DIC can be used to validate the Texas Overlay Tester configuration [63].

In terms of local gradients and isothermal cracking characteristics, Tan and colleagues applied DIC to study the evolution of the strain field in IDT tests [64]. Teguedi et al used DIC to study the thermal strain field to develop during the un-constrained thermal contraction of asphaltic mixtures [65]. Cracking is asphalt is characterized by the formation of a fracture process zone (FPZ) consisting of a meandering primary crack that branches and bridges with secondary and micro-cracks ahead of the crack tip [66]. Many researchers have applied DIC to approximate the size and evolution of the FPZ in mixtures [66]-[69]. An important development is the use of DIC to study the isothermal mechanical fatigue of asphaltic materials [70]-[73].

In term of model validation, DIC is often applied to determine if the heterogeneous asphaltic mixtures can be approximated using continuum mechanics-based models. Various viscoelastic continuum damage (VECD)-based models have been calibrated using DIC [67],[68]. In addition, Birgisson, theorized and validated a new viscoelastic fracture mechanized-based crack growth law using DIC [74],[75].

Beyond DIC, several other optical measurements techniques have been applied to asphaltic mixtures with varying degrees of success including crack counting, crack meandering, 3D-surface scanning, etc. [61], [76], [77],[78].

Reviewing the applications of DIC in asphaltic materials, tests are most often performed under isothermal conditions (i.e. case 1 or case 2). When under non-isothermal conditions, the constitute materials within asphaltic materials do not carry the same thermal expansion and contraction coefficients. As a result, temperature change produces a thermal contraction mismatch within the microstructure and at interfaces making it difficult to separate mechanically and thermally driven strains and stresses. Infrared Thermography has the potential to resolve this problem.

Infrared Thermography (IRT)

Infrared thermography (IRT) is a non-contact experimental technique that enables the measurement of temperature gradients and fields on the surface of objects. The infrared radiation

emitted by objects is detected using a thermographic sensor and processed into thermal images [86]. Infrared thermography is an ideal tool for condition monitoring because it is a non-contact and non-invasive tool that is agnostic to object shape, size, and material type [79]. Infrared thermography is commonly applied in the non-destructive evaluation of buildings, structures, and pavements [80], [81], [82]. It can be utilized in a passive-mode, where the natural temperature gradients are measured and moderate defect detection is possible; or in an active-mode, where a heat pulse is applied to the surface in order to maximize defect detection while losing the natural temperature gradients. In asphaltic mixtures, IRT has been applied to identify thermal segregation during construction and for the detection and characterize surface defects of in-service pavements.

In terms of construction, passive-IRT is often used to identify thermal segregation of the mat (fresh pavement) during compaction. Thermal segregation is the process where localized regions of the mat cool differentially to the main body of the mat. Stroup-Gardiner et al completed a NCHRP project on IRT and found that the nominal temperature of the mat plays a bigger role on particle segregation (density variation) than temperature differentials during compaction [83]. In a follow up 5-year pavement condition survey, Henault and Larsen found that thermal and particle segregation can each exist without the presence of the other and are only co-dependent below threshold nominal temperature and temperature differential values [84]. Using more advanced IRT cameras, Plati et al performed full coverage monitoring of the entire paving and compaction procedure enabling both the identification of thermal segregation but also the detection and monitoring of defects during construction [87]. Analysis of the IRT data lead to an empirical cooling model that estimates the available compaction time.

In terms of flaw detection, both passive- and active-IRT has been applied; however, passive-IRT is easier to apply in the field. Flaw detection is possible due to the increased surface-area at the defect which creates a temperature differential at the defect with respect to the main body. Passive-IRT has been applied for the periodic and continuous monitoring of airport pavements and steel bridge structures respectively with an ASTM standard existing for the later [88], [89], [90]. Sakagami exploited the thermoelastic effect to estimate the stress field and stress

intensity factors near defects using IRT on steel bridges [89]. Solla et al coupled ground penetrating radar (GPR) and IRT for the detection and characterization (width and depth) of defects along a stretch of highway [91]. Dumoilin et al applied active-IRT in the laboratory along with a semi-infinite heat transfer model for the detection of surface and subsurface defects [92], [93].

Automated distress detection using IRT has come into vogue. Oloufa et al performed a study on IRT flaw detection using the software WiseCrax and were able to detect flaws smaller than 1 mm under various field environments (night/day, wet/dry, filled cracks, asphalt joints, etc.) [94]. Conen et al reviewed automated distress detection methods and found for IRT the software Bridgeguard/Roadguard/Flightguard is currently being employed to detect defects in a variety of civil infrastructure [95]. Miah et al recognizing the utility of IRT, recommend the development of a multispectral sensor for road pavement where the data from six sensors (including IRT) are integrated to automatically detect and map flaws along an entire highway [96].

When IRT is coupled with DIC, measurements of the thermomechanical behavior of materials are possible. The strain field can be separated into mechanically and thermally-driven contributions where thermally-driven portion encompasses both internal energy (generated due to deformation) and external heat-sources (from the environment). Chrysochoos and colleagues developed and validated an experimental procedure and mathematical approach for coupled IRT and DIC in homogeneous materials [97]. A similar procedure and validation for heterogenous asphaltic mixtures is needed.

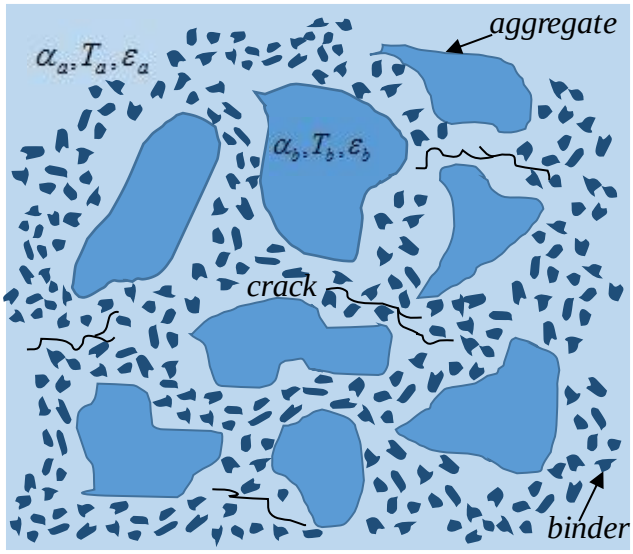

Illustration 3 – Aggregate embedded in an asphalt matrix

Problem Statement

The TSRST test was developed to characterize the low temperature cracking resistance of asphaltic mixtures. Although several researchers have been able to characterize the behavior of asphaltic mixtures with various compositions, binders, air void content, and other factors [47], few researchers have integrated IRT with DIC to observe the evolution of surface temperature gradients and subsequent thermally-induced strains in TSRST specimens. A procedure for coupling IRT and DIC for asphaltic mixtures has yet to be developed [97]. It is hypothesized that an integrated IRT and DIC flaw detection system can elucidate the thermomechanical behavior of asphalt mixtures shown in Illustration 3. This system will provide the empirical evidence necessary to intelligently design asphaltic mixtures to resist low temperature cracking.

Objective

Objective 1 – Develop new technique to analyze thermomechanical behavior of HMA. DIC will be used to measure the local deformation and strain field due to the change of temperature. Coefficient of thermal contraction will be calculated from the thermal strain data. Crack nucleation, propagation, and rupture will be captured to track and calculate thermal crack growth in asphaltic mixtures.

Objective 2 – Characterize low temperature cracking of HMA in the modified TSRST configuration. A single notched prismatic specimen will be used to evaluate fracture mechanics by Linear Elastic Fracture Mechanics (LEFM). IRT will be used to perceive the formulation of thermal cracks using the thermos-elastic effect of Sir. Kelvin and the natural thermal gradients that exist at cracks.

Objective 3 – Develop a method to extract thermal and mechanical behavior to predict HMA response at low temperature. DIC and IRT will be integrated so that the full field thermomechanical behavior on the surface of asphaltic mixtures can be captured.

Material and Test Methods

Material

Specimens in this research will be manufactured according to the Texas Department of Transportation (TxDOT) specifications. Dense-graded hot mixed asphalt (HMAs) materials will be selected for testing. It is commonly called a Type C asphalt material according to the TxDOT, which is mostly available and widely used in West Texas. These materials are collected from Jobe Materials L.P. by Center for Transportation Infrastructure Systems (CTIS) of UTEP and it will be tested according to ASME and AASHTO standard during manufacturing. Superpave performance grade (PG) binder substitution PG 64-22 allows a wide temperature range condition between $-22°C$ to $64°C$ suitable for most region subjected to temperature cycle during the day to night period. The properties of the HMAs are summarized in Table 7 and the gradation is listed in Table 8.

Table 7 – Summary of HMA properties

Properties	Type-C
NMAS (mm)	19
Asphalt Performance Grade	PG 70-22
Binder Substitution	PG 64-22
Optimal Asphalt Content (%)	4.6
Specific Gravity	1.001
Binder Percent (%)	4.6
VMA (%) at optimum AC	15.2

Table 8 – Gradation chart of Type-C mix

Sieve Size	Type-C (Percentage)
1''	100.0
3/4"	99.3
3/8"	82.4
No.4	52.7
No. 8	36.9
No. 30	18.6
No. 50	14.0
No. 200	5.6

Specimen Design and Method

Prior to this SPTC project, Stewart et, el. studied the feasibility to quantify the thermomechanical fatigue and the effect of thickness on fracture resistance of HMAs. In this investigation, low-temperature cracking of HMAs will be evaluated. HMA specimens will be manufactured according to AASHTO T312-15 and ASTM D6928-15 standard. This manufacturing process is well explained in previous research work of this project. Indirect tensile test (IDT), Free thermal contraction test, Thermal Stress Restrain Specimen Test (TSRST), 3D Digital Image Correlation and IR Thermography will be used to analyze the thermomechanical response of HMA in low temperature.

Indirect Tensile Test (IDT) Specimen

The indirect tensile test is widely used to determine fracture strength, energy, and modulus of the specimen. Since, in author's knowledge, the mechanical properties of this particular Type C HMA prepared in CTIS lab is not available for low temperature, Indirect Tensile Test (IDT) will be performed at $25, 5, \text{and} -10°C$ to obtain fracture strength at three different temperature according to ASTM D6931-17 or AASHTO T322. This IDT test done at different temperatures is important to create a master curve for fracture strength at low temperature. Master curve of IDT

strength will provide insight about strain hardening in the material due to low temperature. The IDT strength will be found by the following equation.

$$S_t = \frac{2000 \times P}{\pi \times t \times D} \tag{9}$$

Where, St = IDT strength in kPa, P=Maximum load in N, t = specimen height before tests in mm and D= Specimen diameter in mm

Although IDT test is standardized for operating at a temperature of $25°C$, there is evidence in several works of literature that they have used IDT test to evaluate asphalt mechanical characteristic at low temperature [106], [115]. In this experiment, IDT test will be evaluated to calculate critical tensile stress and dynamic modulus of HMA in those particular temperatures. Figure 18 depicts the IDT test sample preparation and testing procedure which will be followed with DIC to calculate full field and local strain at low temperature. Strain calculation using DIC at low temperature is explained below in experimental procedure section.

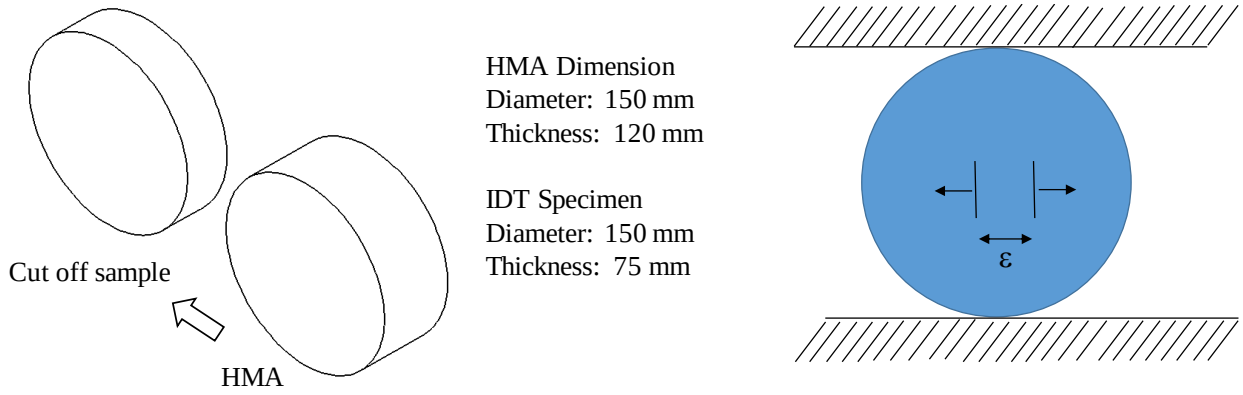

Figure 18 – IDT test specimen

Single Edge Notched Prismatic Specimen

A single edge side notch prismatic specimen will be used to evaluate the low temperature cracking behavior of hot mixed asphalts (HMAs) using classical Linear Elastic Fracture Mechanics (LEFM). Prismatic HMA samples will be prepared from compact HMA sample with a dimension

of 80 mm and 120 mm in length. The side edge single notch will be fabricated by water-cooled saw to avoid unnecessary damage to the specimen according to ASTM 7313-13. This specimen preparation is illustrated in Figure 19.

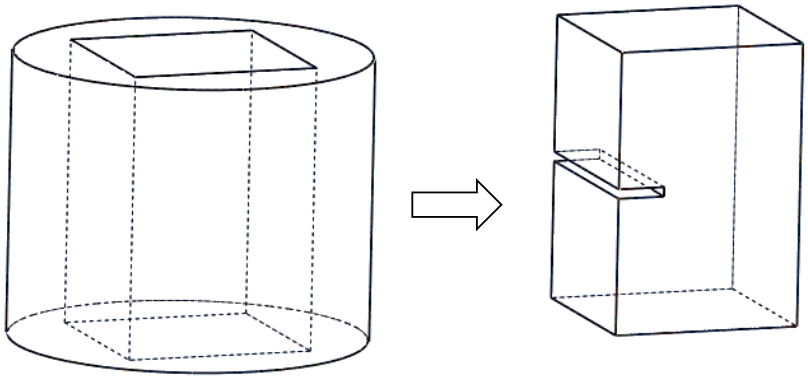

Model Dimension
Length, L: 120 mm
Width, W: 80 mm
Thickness, t: 80 mm
Crack length, a: 20 mm
Crack width : 4 mm

Figure 19 – Single edge notch specimen for modified TSRST test

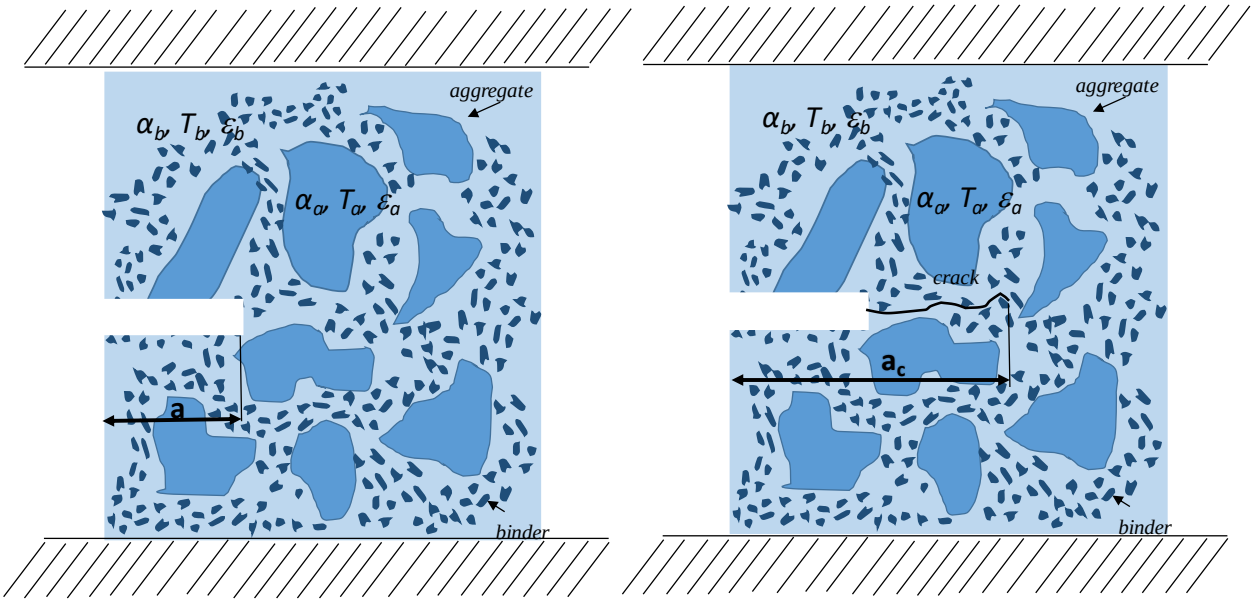

Figure 20 – Specimen preparation (a) HMA with single edge side notch (b) HMA specimen with critical crack length

A notch will be cut at a depth of 20 mm with 4 mm width to maintain the crack length to specimen width ratio within the accepted limit for applying LEFM principle. Since at low-

temperature asphalt materials show viscoelastic property and it is often found strain hardening after the transition temperature, the method of LEFM will be useful for good prediction of fracture at the small fracture process zone. Cohesive crack model (CCM) will be used to evaluate the fracture energy and it can be found as:

$$G_f = \int_0^{\infty} \sigma dw = \int_0^{\infty} f(w) dw \tag{10}$$

Whereas G_f is fracture energy, σ is tensile stress and w is the crack opening displacement.

CCM suitably explains non-linear fracture at the preexisting crack mouth [114]. Stress intensity factor for the single edge notched specimen is given by:

$$K_I = C\sigma\sqrt{\pi a} \tag{11}$$

Where, for small cracks: C=1.12 (considering the absence of the closing effects for single edge notch). However, it can also calculate using the Equation (12) to accuracy to 0.5% for $a/W \leq 0.6$.

$$C = 1.122 - 0.231\left(\frac{a}{W}\right) + 10.550\left(\frac{a}{W}\right)^2 - 21.710\left(\frac{a}{W}\right)^3 + 30.382\left(\frac{a}{W}\right)^4$$

$$K_I = \sigma\sqrt{\pi a}\left\{C = 1.122 - 0.231\left(\frac{a}{W}\right) + 10.550\left(\frac{a}{W}\right)^2 - 21.710\left(\frac{a}{W}\right)^3 + 30.382\left(\frac{a}{W}\right)^4\right\} \tag{12}$$

Fracture energy and stress intensity factor will describe mode I failure for HMA specimen at low temperature cracking. Even though HMA samples are heterogeneous in nature and stress generate randomly at binder aggregate interface, accumulated energy will provide insightful information to analyze this non-linear temperature-dependent fracture with LEFM. Critical crack length can be calculated from the fracture energy and stress intensity factor at low temperature. With this valuable information, a homogeneous model for the HMA fracture can be obtained from the heterogeneous sample. Figure 20 shows the proposed model with the critical crack length. Modified TSRST test with the proposed model will be conducted along with DIC to characterize the fracture process zone. Infrared thermography will be incorporated to obtain thermal mismatch at HMA binder aggregate interface.

Experimental Procedure

Free Thermal Contraction

Hot mixed asphalts (HMAs) exhibit viscoelastic property at both high and low temperature. It is important to measure the thermal expansion or contraction coefficient accurately for the particular HMAs to predict their behavior under thermal stress [117], [109]. Viscoelastic property leads the thermal expansion and contraction coefficients of HMAs as a nonlinear function of temperature [117], [108], [116]. This nonlinear function does not vary with the gradation or asphalt air void content but with aggregate and binder type [108], [116]. A different mixture of asphalt produce different thermal properties and often thermal contraction is found different with thermal expansion for a particular material selection due to nonlinear function [109], [110]. In low-temperature cracking, thermal contraction generates a tensile stress which initiates the crack on the surface. Digital image correlation is one of the widely used techniques which captures full-field strain and deformation of the crack surface without any physical contact. Non-uniform strain distribution of the fracture process zone then will be further analyzed to evaluate the performance of the HMAs [105].

3d Digital Image Correlation

Digital image correlation (DIC) uses different correlation techniques for different challenging working conditions to acquire information regarding displacement, velocity and strain from the deformed target subset [113]. These correlation criteria are chosen depending on the practical application. The potential difference arises to calculate the thermal expansion or contraction when a certain method of correlation criterion is chosen. It is because some criterion depends on the change of lighting condition, brightness, image scale and offset and so on [113], [107]. However, large temperature difference, target image subset, and strain do not have a dominant effect on the calculation of the thermal coefficient of expansion or contraction. In addition, small rigid body rotation can also be neglected while using DIC system as it is removed during strain calculation [107]. Normal strains ($e_{x,}e_{y}$) and shear strain (e_{xy}) are obtained from the

displacement along x-direction and y-direction with DIC system. The thermal coefficient of expansion or contraction can then be calculated as thermal strain per unit temperature [104], [111], [112]

Normalized sum of squared difference criterion (NSSD) used by the DIC system is as follows [113].

$$\chi^2{}_{NSSD} = \sum \left(\frac{\sum F_i G_i}{\sum G_i^{\,2}} G_i - F_i \right)^2 \tag{13}$$

Where F is Gaussian random noise for the reference image and G for the image after displacement

In this investigation, NSSD correlation criterion will be used because it is not affected by the scale of lighting. Stereo camera pair will be used to capture calibration image. VIC Snap 8 application from the Correlated Inc., will be used to record the images of calibration target at different positions and angles. The higher number of images the higher possibility of good calibration is generally observed in good lighting condition. These images will be imported to VIC 3D software to calibrate the DIC stereo camera system. In this calibration process, camera intrinsic properties i.e. center position, focal length, skew, kappa and extrinsic properties such as angles, and distance will be measured and calibrated. Calibration by VIC 3D software will normalize camera pairs intrinsic and extrinsic variables by triangulating camera's position and removing lens distortion from the image. A good calibration can be found when there is sufficient light, stereo cameras are in plane with the target object and when there is good speckle pattern [113].

Speckle pattern will be generated by white enamel paint sprayed over the specimen surface to have a white coating. Then the random speckle pattern over the surface will be generated by the mist of black enamel paint from a painting can. It will be allowed an hour to settle the painting on the surface. Speckle images of the HMA specimen will be captured by VIC Snap 8 using time capture feature at acquisition intervals of 500 ms during the test time period. Two charged coupled device (CCD) cameras and two 1500 lumen LED white lights will be focused on the specimens. The cameras will place on a tripod 1 meter away for the specimen. DIC images will be recorded

at a resolution of 1920x1200. All of these images will be analyzed in pre-calibrated VIC 3D software. This analysis will be performed on a selected area of interest (AOI) where uncertainty internal σ (pixel) will be minimized by choosing appropriate subset size and noise level. Lower the subset size indicates the higher accuracy of the analysis. During strain calculation, Gaussian weights will be used for the subset matching to be center weighted. Lagrangian finite strain tensor will be selected with 8-tap splines interpolation to achieve sub-pixel accuracy. Bad data such as blur, debris, poor lighting will be removed by carefully choosing confidence margin and matchability threshold from correlation program. Finally, projection error will be kept minimum to obtain good correlation result by avoiding motion blur, poor calibration and slack mounting of camera pair.

Indirect Tensile Test (IDT)

The universal testing machine, Instron 5969 will be used with the 3119-609 environmental chamber for the Indirect Tensile Test (IDT) at temperature $25, 5, \text{and } -10°C$, and the modified Thermal Stress Restrain Specimen Test (TSRST) will be continued till specimen begin cracking at low temperature shown in Figure 21. This environmental chamber can operate -100 to $350°C$ temperature range. Eurotherm process controller will be used to control the temperature of the environmental chamber. It will be equipped with liquid nitrogen at 230 psi for the cooling purpose. This tabletop 5969 Instron frame has 50 kN load cell and capable to operate 0.001 to 600 mm/min displacement rate. A safety limit for load and cross head displacement will be imposed to avoid any damage. Three IDT tests will be conducted while Instron reaches those predetermined temperatures at 50 mm/min displacement rate following ASTM D6931-12 standard.

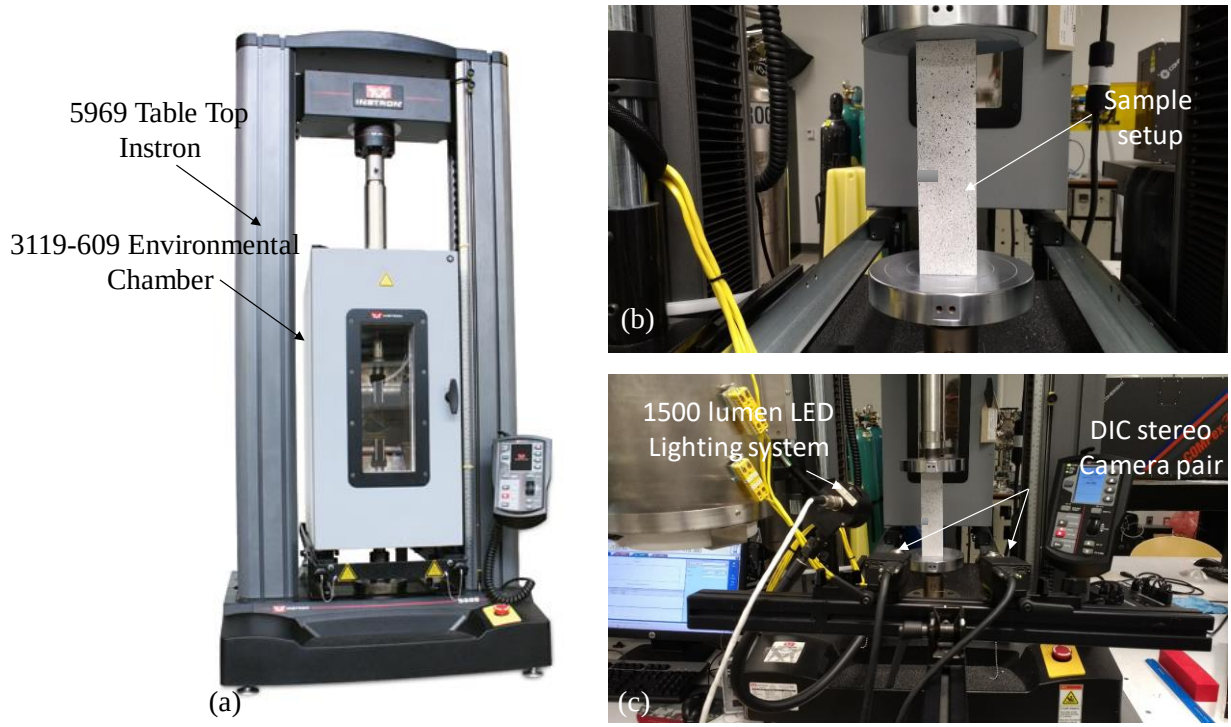

Figure 21 – Testing setup (a) Tabletop 5969 Instron load cell with the 3119-609 environmental chamber, (b) Specimen alignment and (c) DIC system

Thermal contraction coefficient of HMA first will be achieved by free contraction inside the Instron environmental chamber. During free contraction period, continuous images of the deformed surface will be taken by DIC. Further, these images will be processed to obtain linear displacement and velocity along x-axis and y-axis as well as total strain using VIC 3D software system. Rigid body rotation due to free contraction will be considered during thermal contraction coefficient calculation. P Ben et, el. investigated the effect of rigid body rotation and proposed a linear equation to remove its effect from strain calculation [104], [111]. Commercial VIC 3D software from Correlated Solution Inc. can calculate in-plane rotation angle and with its existing function, it can remove this rigid body rotation from the strain. This pure thermal strain will be then plotted with temperature to find the coefficient of thermal contraction for the HMAs.

Notched TSRST

The AASHTO TP-10 method for the TSRST will be used as the basis for the experiments. Three TSRST specimens (single side edge notch prismatic specimens) with the material properties and dimension mentioned above will be manufactured. The test setup of the modified TSRST test for low temperature cracking for HMA type C will be arranged inside Instron environmental chamber. The circular end platens will be cleaned using degreasing agents to clean off the asphalt and sandpaper will be used to clean off the epoxy. J-B weld clear weld epoxy will be used to glue the specimen to the platen. This epoxy has 4400 PSI tensile strength to hold the bond. The specimens will then be glued to platens with an epoxy thickness of 2cm. The specimens will be left 5 mins to set and 1 hour to cure. The platens will be then attached and aligned to a 5969 Instron Loading Frame. A 3119-609 Instron temperature controlled environmental chamber will be used to cool the specimens and apply the cooling at a rate of 10°C/hr [50]. Liquid Nitrogen will be used to cool the HMA specimens shown in Figure 22.

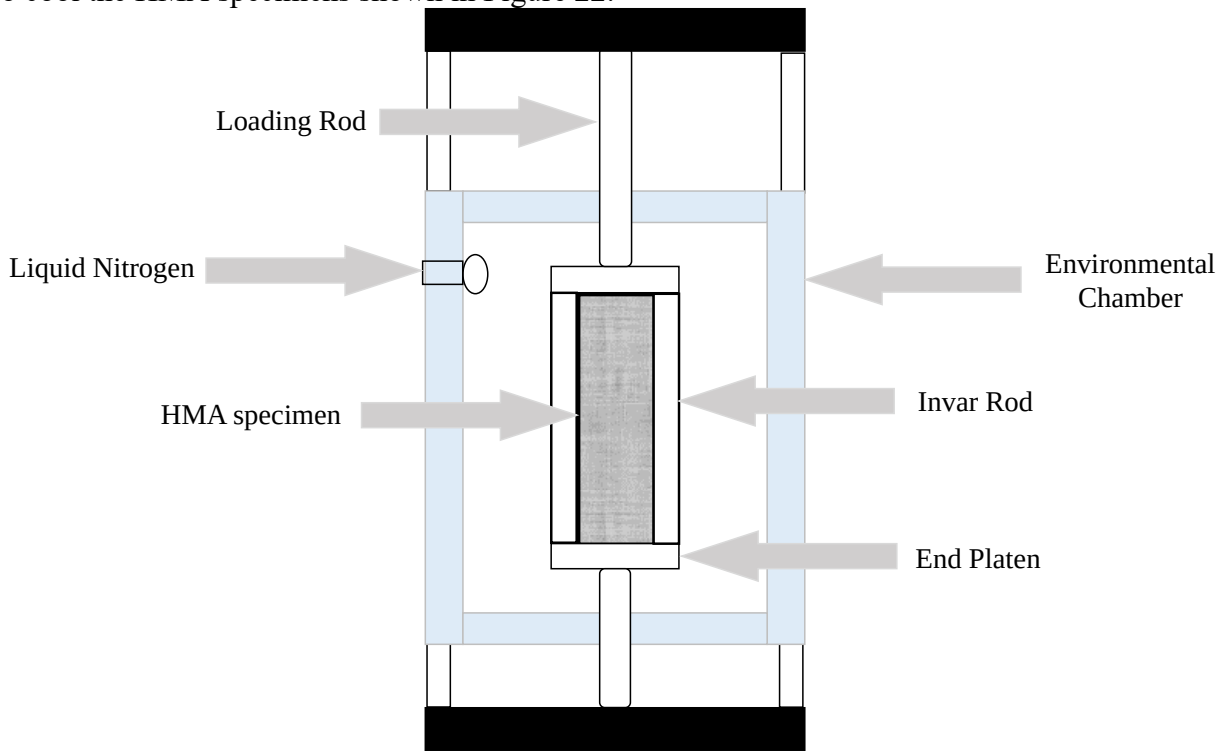

Figure 22 – TSRST Testing Method

An initial load of 44N will be applied to the specimen. Instron Bluehill software will be connected to temperature transducer by computer serial port and will be used to capture stress data generated by HMA specimen during thermal contraction. An Instron program in Bluehill software will be created to report the tensile stress due to thermal contraction. All the dimensions will be plug-in to the Bluehill software for further calculation of stress, strain, modulus and so on. Temperature soaking to $5℃$ for 3 to 4 hrs will be set and k type thermocouple, temperature range -270 to $1372℃$ will be used to record temperature with Instron Bluehill software. Omega temperature controller will be used to record the k type thermocouple reading. The test will be run after the soak temperature. DIC will be used to capture full field deformation for the target samples at 500ms time rate to synchronize with the Instron system. Instron will also be programmed to record temperature data at a similar time rate. While the tests will be running, all the data will be captured with Instron and DIC until the fracture occurs.

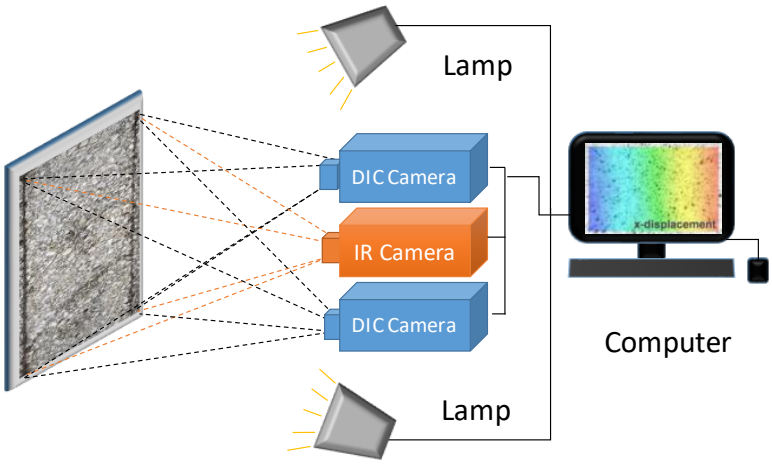

Figure 23 – Schematic of Infrared Thermography

IR Thermography

Infrared Thermography will be paired with the VIC-3D system. The IR system will be set to the same sampling rate in order for the strain captured from the DIC to coincide with the temperature captured from the IR camera. The schematic of the infrared thermography is shown in Figure 23. A FLIR SC7750L thermal imaging camera will be set up on the same tripod as the

DIC cameras. FLIR Research IR software will be used to manipulate and control the camera. The software will be programmed to capture the thermal mismatch along the surface of the specimen test zone as well as capture several temperature readings along different points of the specimen. No calibration of the camera is needed due to the camera being factory calibrated to accurately capture a temperature range of -20°C to 150°C at a pixel resolution of 320x256. After testing, the images and data gathered from the DIC system and IR camera will be exported onto MATLAB to investigate the evolution of thermal stress and temperature gradient due to thermal mismatch, and time.

Laboratory Test Plan

All the tests will be performed using the following test matrix listed in Table 9. For each temperature, three IDT tests will be performed. A total of nine IDT tests in three different temperatures will use to construct the master curve. Each different temperature, DIC will collect reference target images and deformed images data to analyze displacement, strain and fracture process zone. Free thermal contraction test will be performed three times at a temperature rate of $10°C/hr$. In National Pooled Fund Study, Marasteanu articulated the necessity for selecting the proper rate of the change of temperature during the experiment [43], [53]. Thermally induced stress will be determined by notched TSRST test. Three trails will be performed with DIC and IR thermography for modified TSRST. Real-time temperature profiling will further be analyzed to improve HMA performance at low temperature.

Table 9 – Test Matrix

Name of the Tests	Types of equipment	Temperature/ Temp. Range(C)	Preload (kN)	Specimen Dimension (mm)	Air void content (%)	Expected Parameters	No of Trails
Indirect Tensile Test (IDT)	Instron 5969 with 50KN load cell/ MTS 810 Universal Testing System with load cell 11 kip	25, 5, -10	5-10% of expected max load	D = 150±10, t= 75±5	4.6±1	Fracture Strength, Peak load, Modulus of elasticity	9
Free Thermal Contraction	Instron 5969, Environmental Chamber 3119-609, DIC System	25 to -10	X	80X80X120	4.6±1	The coefficient of Thermal Contraction (CTC)	3
Thermal Stress Restrain Specimen Test (TSRST)	Instron 5969 with a 50KN load cell, Environmental Chamber 3119-609 with (-100 to 350 C) Temp. range	Temp rate = 10 C/hr	44 N	80X80X120	4.6±1	Fracture strength, Fracture temp, Slope (dS/dT), Transition temp	3
Digital Image Correlation (DIC)	DIC system	X	X	X	X	Full field displacement, Velocity, Strain, In-plane rotation, the Thermal coefficient of contraction (CTC)	9
Infrared Thermography	Flir IR camera system	5 to -20	X	X	X	Thermal mismatch contour, the Thermal profile on the surface	3

Analysis of Approach

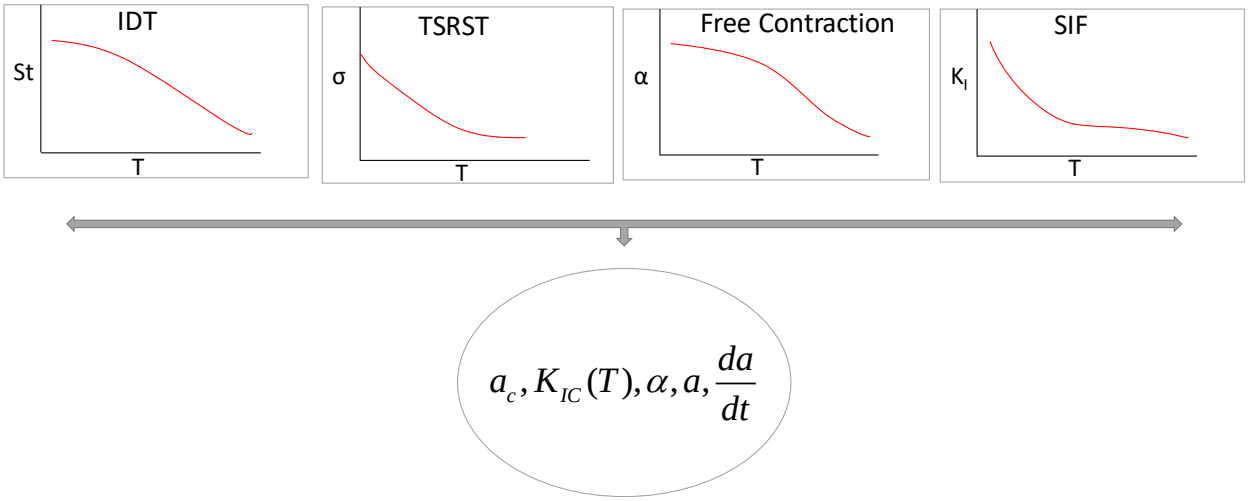

Illustration 4 – Outcomes of the experimental tests

Low-temperature cracking of hot mixed asphalt needs a proper characterization at fracture temperature. Key characterization parameter will be obtained from the above-mentioned test methods. A master curve for fracture strength will be generated for Type C HMA from IDT test. Using this master curve, HMA mechanical properties can be speculated at low temperature. Furthermore, dynamic modulus can also be found from IDT test. Sample material's thermal properties will be determined by free thermal contraction test. The coefficient of thermal contraction (CTC) will be found using digital image correlation technique. Material contracts toward the center and exhibits rigid body rotation while cooling down to low temperature. All these phenomena will be captured and analyzed with DIC to generate mathematical relation of CTC with temperature. A modified TSRST (notched TSRST) will be used to evaluate a single edge notch prismatic specimen fracture behavior at low temperature. This experiment will simulate the preexisting crack on the pavement subjected to low temperature. Fracture strength, fracture temperature, transition temperature from this modified TSRST test will provide important information regarding strain hardening, stress relaxation inside the material. Crack nucleation, micro-crack forming and crack propagation will be found by analyzing the fracture process zone. DIC will capture local full field displacement at fracture process zone. This experiment will help

us to determine various factors associated with HMA while providing sufficient date to build a model to minimize the damage and improve material properties at low temperature. It is hypothesized that critical stress intensity factor and critical crack length will be a temperature dependent parameter. Crack growth rate can also be calculated to obtain knowledge on the types of crack, crack path (single or bifurcate), and time-temperature dependent propagation. All these pieces of knowledge will then be applied to linear elastic fracture mechanics (LEFM). Fracture energy that dominates the local stress near the notch instead of remote stress will be determined by the cohesive crack model (CCM). It will significantly be used to analyze the bond energy between asphalt binder and aggregate. Integration of IR thermography with this experiment will elucidate the thermal profile and thermal mismatch between asphalt binder and aggregate interface. It is speculated that heterogeneity in asphalt will create different thermal and mechanical response when subjected to a thermomechanical load.

Summary and Conclusion

Stochastic nature of HMA stems from the uncertainty regarding the heterogeneous behavior of asphalt, type of asphalt constituents, degree of aging, air void content and so on. These factors lead to non-linear temperature-dependent response while subjected to the low temperature. This study will elucidate stress, deformation, and micro-crack evolution through the state of the art experimental techniques to characterize the mechanical and thermal response of asphalt including two imaging techniques: Digital Image Correlation (DIC) and Infrared Thermography (IRT). Single edge notch prismatic specimen in Thermal Stress Restrain Specimen Test (TSRST) will enable the user to predict the HMA viscoelastic behavior using Linear Elastic Fracture Mechanics (LEFM). Knowledge of Coefficient of Thermal Contraction (CTC), temperature-dependent critical stress intensity factor, and critical crack length will provide valuable insight to characterize HMA's low-temperature performance. Along with mechanical characterization, integrated analysis of kinematical data from DIC and calorimetric data from IRT will enable the user to evaluate stress localization, strain hardening/softening and temperature distribution on the asphalt surface. Finally, this study will unravel the complex interaction of binder aggregate interface and thus will provide scientific evidence to make design decision more accurately for HMA at low temperature.

References

[1] P.W. Cooper, S.R. Kurowski, Introduction to the technology of explosives, VCH, 1996.

[2] C. Siviour, P. Laity, W. Proud, J. Field, D. Porter, P. Church, P. Gould, W. Huntingdon-Thresher, High strain rate properties of a polymer-bonded sugar: their dependence on applied and internal constraints, Proc. R. Soc. A Math. Phys. Eng. Sci. 464 (2008) 1229–1255. doi:10.1098/rspa.2007.0214.

[3] C.M. Cady, C. Liu, P.J. Rae, M.L. Lovato, Thermal and loading dynamics of energetic materials, in: Proc. SEM Annu. Conf., 2009: pp. 1–7.

[4] P. Chen, Z. Zhou, F. Huang, Macro-Micro Mechanical Behavior of a Highly-Particle-Filled Composite Using Digital Image Correlation Method, Advances in Composite Materials - Analysis of Natural and Man-Made Materials, InTech, 2011.

[5] Z. Zhou, P. Chen, F. Huang, S. Liu, Experimental study on the micromechanical behavior of a PBX simulant using SEM and digital image correlation method, Opt. Lasers Eng. 49 (2011) 366–370. doi:10.1016/j.optlaseng.2010.11.001.

[6] Liang, Z., Huang, F., Duan, Z., Zhou, D., Yao, H. (2008). Experiment Study on Impact Damage of PBX Explosive and Simulation Material [J]. Journal of projectiles, rockets, missiles and guidance, 1, 038.

[7] Z. Zhou, P. Chen, Z. Duan, F. Huang, Comparative study of the fracture toughness determination of a polymer-bonded explosive simulant, Eng. Fract. Mech. 78 (2011) 2991–2997. doi:10.1016/j.engfracmech.2011.08.017.

[8] Z. Zhou, P. Chen, F. Huang, Study on dynamic fracture and mechanical properties of a PBX simulant by using dic and SHPB method, in: AIP Conf. Proc., AIP Publishing, 2012: pp. 665–668. doi:10.1063/1.3686366.

[9] C. Liu, C.M. Cady, P.J. Rae, M.L. Lovato, On the Quantitative Measurement of Fracture Toughness in High Explosive and Mock Materials, in: 14th Int. Detonation Symp., 2010: pp. 425–434.

[10] D.M. Williamson, S.J.P. Palmer, W.G. Proud, Fracture studies of PBX simulant materials, AIP Conf. Proc. 845 II (2006) 829–832. doi:10.1063/1.2263450.

[11] L. Ferranti Jr., F.J. Gagliardi, B.J. Cunningham, K.S. Vandersall, Measure Of Quasi-Static Toughness And Fracture Parameters For Mock Explosive And Insensitive High Explosive LX-17, in: 14th Int. Detonation Symp., Coeur d'Alene, ID, 2010.

[12] Z.W. Liu, H.M. Xie, K.X. Li, P.W. Chen, F.L. Huang, Fracture behavior of PBX simulation subject to combined thermal and mechanical loads, Polym. Test. 28 (2009) 627–635. doi:10.1016/j.polymertesting.2009.05.011.

[13] Z. Zhou, P. Chen, Z. Duan, F. Huang, Study on Fracture Behaviour of a Polymer-Bonded Explosive Simulant Subjected to Uniaxial Compression Using Digital Image Correlation Method, Strain. 48 (2012) 326–332. doi:10.1111/j.1475-1305.2011.00826.x.

[14] M. Li, J. Zhang, C.Y. Xiong, J. Fang, J. M Li, Y. Hao, Damage and fracture prediction of plastic-bonded explosive by digital image correlation processing, Opt. Lasers Eng. 43 (2005) 856–868. doi:10.1016/j.optlaseng.2004.09.003.

[15] P.J. Rae, S.J.P. Palmer, H.T. Goldrein, A.L. Lewis, J.E. Field, White-light digital image cross-correlation (DICC) analysis of the deformation of composite materials with random microstructure, Opt. Lasers Eng. 41 (2004) 635–648. doi:10.1016/S0143-8166(02)00179-3.

[16] S.R. Heinz, J.S. Wiggins, Uniaxial compression analysis of glassy polymer networks using digital image correlation, Polym. Test. 29 (2010) 925–932. doi:10.1016/j.polymertesting. 2010.08.001.

[17] S.G. Grantham, C.R. Siviour, W.G. Proud, J.E. Field, High-strain rate Brazilian testing of an explosive simulant using speckle metrology, Meas. Sci. Technol. 15 (2004) 1867–1870. doi:10.1088/0957-0233/15/9/025.

[18] M.A. Sutton, J.J. Orteu, H. Schreier, Image correlation for shape, motion and deformation measurements: Basic concepts, theory and applications, 2009. doi:10.1007/978-0-387-78747-3.

[19] J. Akhavan, The chemistry of explosives, Royal Society of Chemistry, 2011.

[20] Catzin, C.A., Reyes, J.G., Stewart, C.M., 2016,"Manufacturing Method for Mock Polymer Bonded Explosives", MethodsX.(Submitted)

[21] ASTM, D6931-12 Standard Test Method for Indirect Tensile (IDT) Strength of Bituminous Mixtures, (2012). doi: 10.1520/D6931-12

[22] ASTM, D695-15 Standard Test Method for Compressive Properties of Rigid Plastics, (2015). doi: 10.1520/D0695-15.

[23] M. Jerabek, Z. Major, R.W. Lang, Uniaxial compression testing of polymeric materials, Polym. Test. 29 (2010) 302–309. doi:10.1016/j.polymertesting.2009.12.003.

[24] J.R. Rice, P.C. Paris, J.G. Merkle, Some further results of J-integral analysis and estimates, in: ASTM STP 536, 1973: pp. 231–245. doi:10.1520/STP49643S.

[25] ASTM, E1820-15a Standard Test Method for the Measurement of Fracture Toughness, (2015). doi: 10.1520/E1820-15A.

[26] I.L. Lim, I.W. Johnston, S.K. Choi, Stress intensity factors for semi-circular specimens under three-point bending, Eng. Fract. Mech. 44 (1993) 363–382. doi:10.1016/0013-7944(93)90030-V.

[27] J.A. Begley, J.D. Landes, The J integral as a fracture criterion, ASTM STP 514. (1972) 1–20. doi:10.1520/STP514-EB.

[28] Chen, P. W., Huang, F. L., Ding, Y. S., 2007, "Microstructure, deformation and failure of polymer bonded explosives." *J. Mater. Sci.*, **42**(13), pp. 5272-5280.

[29] Chen, P. W., Xie, H. M., Huang, F. L. et al., 2006, "Deformation and failure of polymer bonded explosives under diametric compression test." *Polymer Testing*, **3**(25), pp. 333-341.

[30] Banerjee, B., Cady, C. M., and Adams, D. O., 2003, "Micromechanics simulations of glass-estane mock polymer bonded explosives," *Modelling and Simulation in Materials Science and Engineering,* **11**(4), pp. 457–475.

[31] D. M. HOFFMAN, BRUCE J. CUNNINGHAM & TRI D. TRAN (2003) “Mechanical Mocks for Insensitive High Explosives,” *Journal of energetic Materials*, 21:4, pp. 201-222.

[32] Yong, Y., Zhang, J., and Zhang, J., 2009, "A modified Brazilian disk tension test." *International Journal of Rock Mechanics and Mining Sciences*, **46**(2), pp. 421-425.

[33] Hondros, G., 1959, "The evaluation of Poisson’s ratio and the modulus of materials of a low tensile resistance by the Brazilian (indirect tensile) test with particular reference to concrete." *Australian Journal of Applied Science*, **10**(3), pp. 243-268.

[34] Huang, B., Shu, X., and Tang, Y., 2005, “Comparison of Semi-Circular Bending and Indirect Tensile Strength Tests for HMA Mixtures.” *Advances in Pavement Engineering*, pp. 1-12.doi: 10.1061/40776(155)14.

[35] Mellor, M., and Hawkes, I., 1971, "Measurement of tensile strength by diametral compression of discs and annuli." *Engineering Geology*, **5**(3), pp. 173-225.

[36] Kim, Y., Seo, Y., King, M., and Momen, M., 2004, "Dynamic modulus testing of asphalt concrete in indirect tension mode." *Transportation Research Record: Journal of the Transportation Research Board*, **1891**, pp. 163-173.

[37] Fairhurst, C., 1964, "On the validity of the ‘Brazilian’ test for brittle materials, “International *Journal of Rock Mechanics and Mining Sciences,* **1**(4), pp. 535-546.

[38] Liu, C., 2010, "Elastic constants determination and deformation observation using Brazilian disk geometry." *Experimental mechanics*, 50(7), pp. 1025-1039.

[39] C. Liu & D.G. Thompson (2012) Deformation and failure of a heterogeneous high explosive, Philosophical Magazine Letters, 92:8, 352-361, DOI:10.1080/09500839. 2012.673021

[40] Cady, C. M. et al, 1998, “High and Low strain rate compression properties of several energetic material composites as a function of Strain Rate and temperature,” C. Of, S. Energetic, M. Composites, vol. 836.

[41] Baytos, J. F. (1980). LASL explosive property data (Vol. 4). Univ of California Press.

[42] AASHTO TP 105-13. 2013.Standard Method for Determining the Fracture Energy of Asphalt Mixtures Using the Semi Circular Bend Geometry (SCB). American Association of State Highway and Transportation Officials, Washington, DC.

[43] Marasteanu, M. O., Li, X., Clyne, T. R., Voller, V., Timm, D. H., & Newcomb, D. (2004). Low Temperature Cracking of Asphalt Concrete Pavement.

[44] Brown, E. R., Kandhal, P. S., & Zhang, J. (2001). Performance Testing For Hot Mix Asphalt. National Center for Asphalt Technology.

[45] Farrar, M. J., Hajj, E. Y., Planche, J. P., & Alavi, M. Z. (2013). A method to estimate the thermal stress build-up in an asphalt mixture from a single-cooling event. Road Materials and Pavement Design, 14(sup1), 201-211.

[46] Li, X. J., & Marasteanu, M. O. (2010). Using semi-circular bending test to evaluate low temperature fracture resistance for asphalt concrete. Experimental mechanics, 50(7), 867-876.

[47] Li, X., Braham, A. F., Marasteanu, M. O., Buttlar, W. G., & Williams, R. C. (2008). Effect of factors affecting fracture energy of asphalt concrete at low temperature. Road materials and pavement design, 9(sup1), 397-416.

[48] Fortier, R., & Vinson, T. S. (1998). Low Temperature Cracking and Aging Performance of Modified Asphalt Concrete Specimens. Transportation Research Record: Journal of the Transportation Research Board.

[49] Velasquez, R., & Bahia, H. (2013). Critical factors affecting thermal cracking of asphalt pavements: towards a comprehensive specification. Road Materials and Pavement Design, 14(sup1), 187-200.

[50] Jung, D. H., & Vinson, T. S. (1994). Low Temperature Cracking: Test Selection. Washington D.C: SHRP.

[51] Kanerva, H. K., Vinson, T. S., & Zeng, H. (1994). Low-Temperature Cracking: Field Validation of the Thermal Stress Restrained Specimen Test. Washington D.C: Strategic Highway Research Program.

[52] Kim, S.-S. (2005). Direct Measurement of Asphalt Binder Thermal Cracking. Journal of Materials in Civil Engineering.

[53] Marasteanu, M., Zofka, A., Turos, M., Li, X., Velasquez, R., & Li, X. (2007). Investigation of Low Temperature Cracking in Asphalt Pavements. Minnesota Department of Transportaion.

[54] Sebaaly, P. E., Lake, A., & Epps, J. (2002). Evaluation of Low-Temperature Properties of HMA Mixtures. Journal of Transportation Engineering.

[55] Braham, A., Buttlar, W., & Marasteanu, M. (2007). Effect of binder type, aggregate, and mixture composition on fracture energy of hot-mix asphalt in cold climates. Transportation Research Record: Journal of the Transportation Research Board, (2001), 102-109.

[56] Romero, P., Youtcheff, J., & Stuart, K. (1999). Low-temperature physical hardening of hot-mix asphalt. Transportation Research Record: Journal of the Transportation Research Board, (1661), 22-26.

[57] Pan, B. (2011). Recent progress in digital image correlation. Experimental Mechanics, 51(7), 1223-1235.

[58] Roux, S., Réthoré, J., & Hild, F. (2009). Digital image correlation and fracture: an advanced technique for estimating stress intensity factors of 2D and 3D cracks. Journal of Physics D: Applied Physics, 42(21), 214004.

[59] Romeo, E. (2013). Two-dimensional digital image correlation for asphalt mixture characterisation: interest and limitations. Road Materials and Pavement Design, 14(4), 747-763.

[60] Kim, Y. R., & Wen, H. (2002). Fracture energy from indirect tension testing. Asphalt Paving Technology, 71, 779-793.

[61] Stewart, C. M., Oputa, C. W., & Garcia, E. (2018). Effect of specimen thickness on the fracture resistance of hot mix asphalt in the disk-shaped compact tension (DCT) configuration. Construction and Building Materials, 160, 487-496.

[62] Montepara, A., Romeo, E., Isola, M., & Tebaldi, G. (2011). The role of fillers on cracking behavior of mastics and asphalt mixtures. Journal of the Association of Asphalt Paving Technologists, 80.

[63] Ramos, E., Gutierrez, A., Tirado, C., Stewart, C., Abdallah, I., & Nazarian, S. (2016). Explaining Overlay Tester Results with Digital Image Correlation and Finite Element Analysis. In International Conference on Transportation and Development 2016 (pp. 884-894).

[64] Yi-qiu, T., Lei, Z., Meng, G., & Li-yan, S. (2012). Investigation of the deformation properties of asphalt mixtures with DIC technique. Construction and Building Materials, 37, 581-590.

[65] Teguedi, M. C., Blaysat, B., Toussaint, E., Moreira, S., Liandrat, S., & Grédiac, M. (2016). Applying a full-field measurement technique for studying the local deformation in reclaimed asphalt pavements. Construction and Building Materials, 121, 547-558.

[66] Trivedi, N., Singh, R. K., & Chattopadhyay, J. (2015). Investigation on fracture parameters of concrete through optical crack profile and size effect studies. Engineering Fracture Mechanics, 147, 119-139.

[67] Seo, Y. (2003). A comprehensive study of crack growth in asphalt concrete using fracture mechanics.

[68] Chehab, G. R., Seo, Y., & Kim, Y. R. (2007). Viscoelastoplastic damage characterization of asphalt–aggregate mixtures using digital image correlation. International Journal of Geomechanics, 7(2), 111-118.

[69] Hill, B., & Buttlar, W. G. (2016). Evaluation of polymer modification in asphalt mixtures through digital image correlation and performance space diagrams. Construction and Building Materials, 122, 667-673.

[70] Read, J. M. (1996). Fatigue cracking of bituminous paving mixtures (Doctoral dissertation, University of Nottingham).

[71] Hartman, A. M., & Gilchrist, M. D. (2004). Evaluating four-point bend fatigue of asphalt mix using image analysis. Journal of materials in civil engineering, 16(1), 60-68.

[72] Birgisson, B., Montepara, A., Romeo, E., Roque, R., & Tebaldi, G. (2010). Influence of mixture properties on fracture mechanisms in asphalt mixtures. Road Materials and Pavement Design, 11(sup1), 61-88.

[73] Gao, L., Ni, F., Ling, C., & Yan, J. (2016). Evaluation of fatigue behavior in cold recycled mixture using digital image correlation method. Construction and Building Materials, 102, 393-402.

[74] Birgisson, B., Montepara, A., Romeo, E., Roque, R., Roncella, R., & Tebaldi, G. (2007). Determination of fundamental tensile failure limits of mixtures. Asphalt Paving Technology-Proceedings, 76, 303.

[75] Birgisson, B., Montepara, A., Romeo, E., Roque, R., & Tebaldi, G. (2010). Influence of mixture properties on fracture mechanisms in asphalt mixtures. Road Materials and Pavement Design, 11(sup1), 61-88.

76] Braz, D., Lopes, R. T., & Motta, L. M. G. (2004). Research on fatigue cracking growth parameters in asphaltic mixtures using computed tomography. Nuclear Instruments and Methods in Physics Research Section B: Beam Interactions with Materials and Atoms, 213, 498-502.

[77] Nguyen, M. T., Lee, H. J., & Baek, J. (2012). Fatigue analysis of asphalt concrete under indirect tensile mode of loading using crack images. Journal of Testing and Evaluation, 41(1), 148-158.

[78] Muniandy, R., Akhir, N. A. B. C. M., Hassim, S., & Moazami, D. (2014). Laboratory fatigue evaluation of modified and unmodified asphalt binders in stone mastic asphalt mixtures using a newly developed crack meander technique. International Journal of Fatigue, 59, 1-8.

[79] Bagavathiappan, S., Lahiri, B. B., Saravanan, T., Philip, J., & Jayakumar, T. (2013). Infrared thermography for condition monitoring–A review. Infrared Physics & Technology, 60, 35-55.

[80] Wiggenhauser, H. (2002). Active IR-applications in civil engineering. Infrared Physics & Technology, 43(3-5), 233-238.

[81] Kylili, A., Fokaides, P. A., Christou, P., & Kalogirou, S. A. (2014). Infrared thermography (IRT) applications for building diagnostics: A review. Applied Energy, 134, 531-549.

[82] Goel, A., & Das, A. (2008). Nondestructive testing of asphalt pavements for structural condition evaluation: a state of the art. Nondestructive Testing and Evaluation, 23(2), 121-140.

[83] Stroup-Gardiner, M., Law, M., & Nesmith, C. (2000). Using infrared thermography to detect and measure segregation in hot mix asphalt pavements. International journal of pavement engineering, 1(4), 265-284.

[84] Henault, J., & Larsen, D. (2006). Thermal imaging of hot-mix asphalt paving projects in Connecticut. Transportation Research Record: Journal of the Transportation Research Board, (1946), 130-138.

[85] Teguedi, M. C., Toussaint, E., Blaysat, B., Moreira, S., Liandrat, S., & Grédiac, M. (2017). Towards the local expansion and contraction measurement of asphalt exposed to freeze-thaw cycles. Construction and Building Materials, 154, 438-450.

[86] Nandhakumar, N., & Aggarwal, J. K. (1988). Integrated analysis of thermal and visual images for scene interpretation. IEEE Transactions on Pattern Analysis and Machine Intelligence, 10(4), 469-481.

[87] Plati, C., Georgiou, P., & Loizos, A. (2014). Use of infrared thermography for assessing HMA paving and compaction. Transportation Research Part C: Emerging Technologies, 46, 192-208.

[88] Moropoulou, A., Avdelidis, N. P., Koui, M., & Kakaras, K. (2001). An application of thermography for detection of delaminations in airport pavements. NDT & E International, 34(5), 329-335.

[89] Sakagami, T. (2015). Remote nondestructive evaluation technique using infrared thermography for fatigue cracks in steel bridges. Fatigue & Fracture of Engineering Materials & Structures, 38(7), 755-779.

[90] ASTM International. (2013). ASTM D4788-03(2013) Standard Test Method for Detecting Delaminations in Bridge Decks Using Infrared Thermography.

[91] Solla, M., Lagüela, S., González-Jorge, H., & Arias, P. (2014). Approach to identify cracking in asphalt pavement using GPR and infrared thermographic methods: Preliminary findings. Ndt & E International, 62, 55-65.

[92] Dumoulin, J., Ibos, L., Ibarra-Castanedo, C., Mazioud, A., Marchetti, M., Maldague, X., & Bendada, A. (2010). Active infrared thermography applied to defect detection and characterization on asphalt pavement samples: comparison between experiments and numerical simulations. Journal of modern optics, 57(18), 1759-1769.

[93] Dumoulin, J., Ibos, L., Marchetti, M., & Mazioud, A. (2011). Detection of non emergent defects in asphalt pavement samples by long pulse and pulse phase infrared thermography. European Journal of Environmental and Civil Engineering, 15(4), 557-574.

[94] Oloufa, A., Mahgoub, H., & Ali, H. (2004). Infrared thermography for asphalt crack imaging and automated detection. Transportation Research Record: Journal of the Transportation Research Board, (1889), 126-133.

[95] Coenen, T. B., & Golroo, A. (2017). A review on automated pavement distress detection methods. Cogent Engineering, 4(1), 1374822.

[96] Miah, S., Uus, A., Liatsis, P., Roberts, S., Twist, S., Hovens, M., & Godding, H. (2015, September). Design of multidimensional sensor fusion system for road pavement inspection. In Systems, Signals and Image Processing (IWSSIP), 2015 International Conference on (pp. 304-308). IEEE.

[97] Chrysochoos, A., Huon, V., Jourdan, F., Muracciole, J. M., Peyroux, R., & Wattrisse, B. (2010). Use of full-field digital image correlation and infrared thermography measurements for the thermomechanical analysis of material behaviour. Strain, 46(1), 117-130.

[98] Henault, J., & Larsen, D. (2006). Thermal imaging of hot-mix asphalt paving projects in Connecticut. Transportation Research Record: Journal of the Transportation Research Board, (1946), 130-138.

[99] AASHTO T322, 2004, "Standard Test Method for Determining the Creep Compliance and Strength of Hot Mix Asphalt (HMA) Using the Indirect Tensile Test Device, "American Association of State Highway and Transportation Officials (AASHTO), Washington, DC, 24th ed.

[100] AASHTO, T. (2006). 313-02. *Determining the flexural creep stiffness of asphalt binder using the Bending Beam Rheometer (BBR), American Association of State Highway and Transportation Officials*.

[101] ASTM, D. (2008). 6648 (2001) Standard Test Method for Determining the Flexural Creep Stiffness of Asphalt Binder Using the Bending Beam Rheometer. *Annual Book of ASTM Standards*, *4*.

[102] AASHTO TP 125, 2016, Provisional Method of Test for Determining the Flexural Creep Stiffness of Asphalt Mixtures Using the Bending Beam Rheometer (BBR), American Association of State Highway and Transportation Officials, Washington, DC.

[103] TP10, A. D. (1993). Standard test method for thermal stress restrained specimen tensile strength. *American Association of State Highway and Transportation Officials*.

[104] Bing, P., Hui-min, X., Tao, H., & Asundi, A. (2009). Measurement of coefficient of thermal expansion of films using digital image correlation method. Polymer Testing, 28(1), 75-83.

[105] Buttlar, W. G., Hill, B. C., Kim, Y. R., Kutay, M. E., Millien, A., Montepara, A., . . . Romeo, E. (2014). Digital image correlation techniques to investigate strain fields and cracking phenomena in asphalt materials. Materials and Structures, 47(8), 1373-1390.

[106] Christensen, D. W., & Bonaquist, R. F. (2004). Evaluation of indirect tensile test (IDT) procedures for low-temperature performance of hot mix asphalt Transportation Research Board.

[107] De Strycker, M., Schueremans, L., Van Paepegem, W., & Debruyne, D. (2010). Measuring the thermal expansion coefficient of tubular steel specimens with digital image correlation techniques. Optics and Lasers in Engineering, 48(10), 978-986.

[108] Islam, M. R., & Tarefder, R. A. (2015). Coefficients of thermal contraction and expansion of asphalt concrete in the laboratory. Journal of Materials in Civil Engineering, 27(11), 04015020.

[109] Jones, G. M., Darter, M. I., & Littlefield, G. (1968). Thermal expansion-contraction of asphaltic concrete.

[110] Littlefield, G. (1967). Thermal expansion and contraction characteristics-utah asphalt concretes. Paper presented at the Assoc Asphalt Paving Technol Proc,

[111] Pan, B., Qian, K., Xie, H., & Asundi, A. (2009). Two-dimensional digital image correlation for in-plane displacement and strain measurement: A review. Measurement Science and Technology, 20(6), 062001.

[112] Pan, B., Wu, D., Wang, Z., & Xia, Y. (2010). High-temperature digital image correlation method for full-field deformation measurement at 1200 C. Measurement Science and Technology, 22(1), 015701.

[113] Schreier, H., Orteu, J., & Sutton, M. A. (2009). Image correlation for shape, motion and deformation measurements Springer US.

[114] Seo, Y. (2003). A comprehensive study of crack growth in asphalt concrete using fracture mechanics.

[115] Vasconcelos, K. L., Bernucci, L. B., & Chaves, J. M. (2012). Effect of temperature on the indirect tensile strength test of asphalt mixtures. Paper presented at the Proceedings, 5 Th Eurasphalt and Eurobitume Congress,

[116] Xu, Q., & Solaimanian, M. (2007). Measurement and evaluation of asphalt concrete thermal expansion and contraction. Journal of Testing and Evaluation, 36(2), 140-149.

[117] Zeng, M., & Shields, D. H. (1999). Nonlinear thermal expansion and contraction of asphalt concrete. Canadian Journal of Civil Engineering, 26(1), 26-34.

Vita

Md Fazle Rabbi had started his Bachelor of Science in Mechanical Engineering from the Khulna University of Engineering & Technology (KUET), Khulna, Bangladesh in the year 2005. From the onset of his undergraduate studies, he achieved the University Merit Scholarship consecutive four years and obtain a merit position 2nd among 113 successful graduates on April 19, 2010. Soon after the graduation, he worked for the industries for two years and later on, he started his career to the Khulna University of Engineering & Technology (KUET) as a Lecturer in the Department of Mechanical Engineering. During his tenure, he mentored students in their class, project/ thesis, and served in different administrative positions at KUET. In the year 2016, he applied to the graduate program of UTEP and joined to the Materials at Extreme Research Group under the supervision of Dr. Calvin M. Stewart. Here, he successfully completed a project on Energetic Materials supported by Sandia National Laboratory. He contributed to developing a standard test procedure for the energetic material (polymer-bonded explosive, PBX simulant) of varying compositions and subjected to aging by investigating the fracture resistance of PBXs. His work with Sandia was published in U.S. Department of Energy, Office of Scientific and Technical Information. Later part of his research, he prepared a proposal plan funded by Southern Plains Transportation Center to elucidate HMAs thermomechanical response at low temperature. At present, he is planning to pursue his Ph.D. in Mechanical Engineering at Arizona State University from the August 2018.

Contact Information: fazlerbb@gmail.com

This Thesis was typed by Md Fazle Rabbi